10-2-2022

Hydrogen isotope behavior during rhyolite glass hydration under hydrothermal conditions

Michael R. Hudak

Ilya N. Bindeman

James M. Watkins

Jacob B. Lowenstern

Geochimica et Cosmochimica Acta 337 (2022) 33–48

Contents lists available at ScienceDirect

Geochimica et Cosmochimica Acta

journal homepage: www.elsevier.com/locate/gca

Hydrogen isotope behavior during rhyolite glass hydration under hydrothermal conditions

Michael R. Hudak [a,b,*], Ilya N. Bindeman [a], James M. Watkins [a], Jacob B. Lowenstern [c]

[a] Department of Earth Sciences, 1272 University of Oregon, Eugene, OR 97403, United States
[b] Marine Chemistry and Geochemistry Department, Woods Hole Oceanographic Institution, Woods Hole, MA 02543, United States
[c] U.S. Geological Survey, David A. Johnston Cascades Volcano Observatory, 1300 SE Cardinal Court, Vancouver, WA 98683, United States

ARTICLE INFO

Article history:
Received 28 January 2021
Accepted 24 September 2022
Available online 2 October 2022
Associate editor: Lawrence M Anovitz

Keywords:
Hydrogen isotopes
Silicic glass
Glass hydration
H_2O species
Diffusion modeling

ABSTRACT

The diffusion of molecular water (H_2O_m) from the environment into volcanic glass can hydrate the glass up to several wt% at low temperature over long timescales. During this process, the water imprints its hydrogen isotope composition (δD_{H2O}) to the glass (δD_{gl}) offset by a glass-H_2O fractionation factor ($\Delta D_{gl\text{-}H2O} = \delta D_{gl} - \delta D_{H2O}$) which is approximately −33‰ at Earth surface temperatures. Glasses hydrate much more rapidly at higher, sub-magmatic temperatures as they interact with H_2O during eruption, transport, and emplacement. To aid in the interpretation of δD_{gl} in natural samples, we present hydrogen isotope results from vapor hydration experiments conducted at 175–375 °C for durations of hours to months using natural volcanic glasses. The results can be divided into two thermal regimes: above 250 °C and below 250 °C. Lower temperature experiments yield raw $\Delta D_{gl\text{-}H2O}$ values in the range of −33 ± 11‰. Experiments at 225 °C using both positive and negative initial $\Delta D_{gl\text{-}H2O}$ values converge on this range of values, suggesting this range represents the approximate equilibrium fractionation for H isotopes between glass and H_2O vapor ($10^3 ln\alpha_{gl\text{-}H2O}$) below 250 °C. Variation in $\Delta D_{gl\text{-}H2O}$ (−33 ± 11‰) between different experiments and glasses may arise from incomplete hydration, analytical uncertainty, differences in glass chemistry, and/or subordinate kinetic isotope effects. Experiments above 250 °C yield unexpectedly low δD_{gl} values with $\Delta D_{gl\text{-}H2O}$ values of ≤−85‰. While alteration alone is incapable of explaining the data, these run products have more extensive surface alteration and are not interpreted to reflect equilibrium fractionation between glass and H_2O vapor. Fourier transform infrared spectroscopy (FTIR) shows that glass can hydrate with as much as 5.9 wt% H_2O_m and 1.0 wt% hydroxl (OH^-) in the highest P-T experiment at 375 °C and 21.1 MPa. Therefore, we employ a 1D isotope diffusion–reaction model of glass hydration to evaluate the roles of equilibrium fractionation, isotope diffusion, water speciation reactions internal to the glass, and changing boundary conditions (e.g. alteration and dissolution). At lower temperatures, the best fitting model results to experimental data for low silica rhyolite (LSR) glasses require only an equilibrium fractionation factor and yield $10^3 ln\alpha_{gl\text{-}H2O}$ values of −33‰ ± 5‰ and −25‰ ± 5‰ at 175 °C and 225 °C, respectively. At higher temperatures, $\Delta D_{gl\text{-}H2O}$ is dominated by boundary layer effects during glass hydration and glass surface alteration. The modeled bulk δD_{gl} value is highly responsive to changes in the δD_{gl} boundary condition regardless of the magnitude of other kinetic effects. Observed glass dissolution and surficial secondary mineral formation are likely to impose a disequilibrium boundary layer that drives extreme δD_{gl} fractionation with progressive glass hydration. These results indicate that the observed $\Delta D_{gl\text{-}H2O}$ of ~−33 ± 11‰ can be cautiously applied as an equilibrium $10^3 ln\alpha_{gl\text{-}H2O}$ value to natural silicic glasses hydrated below 250 °C to identify hydration sources. This approximate $\Delta D_{gl\text{-}H2O}$ may be applicable to even higher temperature glasses hydrated on short timescales (of seconds to minutes) in phreatomagmatic or submarine eruptions before H_2O in the glass is primarily affected by boundary layer effects associated with alteration on the glass surface.

1. Introduction

Water is abundant both at Earth's surface, in the crust, and in its deep interior. As the most abundant volcanic volatile and the primary driver of volcanic eruptions, the solubility, diffusivity,

* Corresponding author at: Marine Chemistry and Geochemistry Department, Woods Hole Oceanographic Institution, Woods Hole, MA 02543, United States.
E-mail address: michael.hudak@whoi.edu (M.R. Hudak).

https://doi.org/10.1016/j.gca.2022.09.032
0016-7037/

and speciation of H_2O in silicate melts have been thoroughly investigated at magmatic temperatures over a large range of compositions in natural samples and in experiments (Stolper, 1982; Silver et al., 1990; Zhang et al., 1991; Zhang et al., 1997; Withers et al., 1999; Zhang, 1999; Zhang and Behrens, 2000; Newman and Lowenstern, 2002; Liu et al., 2005; Ni and Zhang, 2008; Coumans et al., 2020). Volcanic glasses that have rehydrated in the environment after eruption and deposition have provided complementary constraints on these properties of H_2O in glass at low temperatures (Friedman and Long, 1976; Anovitz et al., 2008; Giachetti et al., 2015).

Hydrogen isotope studies of hydrous volcanic glasses have provided insights into the behavior of water during volcanic degassing and post-eruptive hydration, sometimes referred to as secondary hydration (Seligman et al., 2016; Martin et al., 2017; Giachetti et al., 2020). These two processes occur at very different temperatures, which results in in the application of hydrogen isotopes in volcanic glass to vastly different timescales (Fig. 1). At higher temperatures (>500 °C), obsidian pyroclasts and flows become isotopically lighter with progressive degassing and H_2O loss, and these trends can be modeled to probe degassing phenomena and fluid compositions over timescales of just minutes or hours (e.g. Taylor et al., 1983; Newman et al., 1988; Dobson et al., 1989; Castro et al., 2014; Seligman et al., 2016; Walter and Castro, 2020). Degassed glass hydrated in the surficial environment (<40 °C) records the composition of the local meteoric water, making δD in glass (δD_{gl}) a viable paleoclimate proxy (e.g. Cassel et al., 2014, 2012,2009; Colwyn and Hren, 2019; Dettinger and Quade, 2015; Friedman et al., 1993b; Hudak and Bindeman, 2018; Jackson et al., 2019; Seligman et al., 2016).

While the behavior of H_2O and its isotopes in volcanic glass at magmatic temperatures and ambient temperature is fairly well understood, considerably less is known about the rates, mechanisms, and isotopic signatures of glass hydration at intermediate temperatures between 100 and 500 °C (Friedman and Long, 1976; Mazer et al., 1991; Anovitz et al., 2004; Hudak and Bindeman, 2020). Both H_2O_m and OH^- are present as dissolved species in silicate glasses and melts, but H_2O_m is the diffusive species at all temperatures (e.g. Zhang et al., 1991; Behrens et al., 2007; Hudak and Bindeman, 2020). However, a critical difference between glasses and melts is the ability of H_2O to repartition into OH^-. The equilibrium speciation in melts is known at $T > 400$ °C as a function of total water (H_2O_t) concentration and bulk composition (Stolper, 1982; Silver et al., 1990; Zhang et al., 1997; Ihinger et al., 1999; Withers et al., 1999; Newman and Lowenstern, 2002; Coumans et al., 2020). Generally, this reaction is not thought to proceed below the glass transition temperature (T_g), which is the temperature at which liquid melt begins to exhibit the mechanical and thermodynamic properties of a solid glass. The T_g is a function of bulk composition, cooling rate, and volatile concentration, and is generally $\geq$ 400 °C (e.g. Dingwell, 1995; Dingwell et al., 1996; Dingwell, 1998; Giordano et al., 2005; Del Gaudio et al., 2007). Understanding the formation of OH^- in glasses is critical for interpreting hydrogen isotope compositions in volcanic glass during cooling and hydration because hydrogen isotope fractionation between melt and H_2O vapor at magmatic conditions is strongly dependent on the proportion of OH^- to H_2O_m (Dobson et al., 1989). At low temperatures, H_2O_m respeciation to OH^- is extremely slow so the glass-H_2O fractionation depends solely on H_2O_m during rehydration.

All melts must cool below T_g and through the temperature window between magmatic and ambient conditions. Even at fast quench rates, interactions and reactions between H_2O vapor and a melt or glass are possible on short timescales and length scales because of the high D_{H2O} at near-magmatic temperatures (Fig. 1). More extensive hydration at long timescales are necessary to attain chemical and isotopic equilibrium, and the experimental glasses presented herein benefit from having been previously characterized and interpreted to constrain H_2O diffusivity and solubility (Hudak and Bindeman, 2020). A critical aspect of chemical equilibrium to understand is the reaction rate between H_2O_m and OH^- within the glass as this may affect hydrogen isotope fractionation. Reactions and hydrogen isotope partitioning between these species at high, but sub-magmatic (hydrothermal) temperatures below T_g must be better understood to interpret the record of H_2O in volcanic glass. This study combines glass hydration experiments, bulk hydrogen isotope measurements, and a new isotope diffusion–reaction model to investigate partitioning between H_2O_m and OH^- in glass and how this reaction affects the hydrogen isotope composition of the glass.

2. Methods

2.1. Experimental materials and design

Glass hydration experiments were conducted over a hydrothermal temperature range from 175 °C to 375 °C (and isochoric

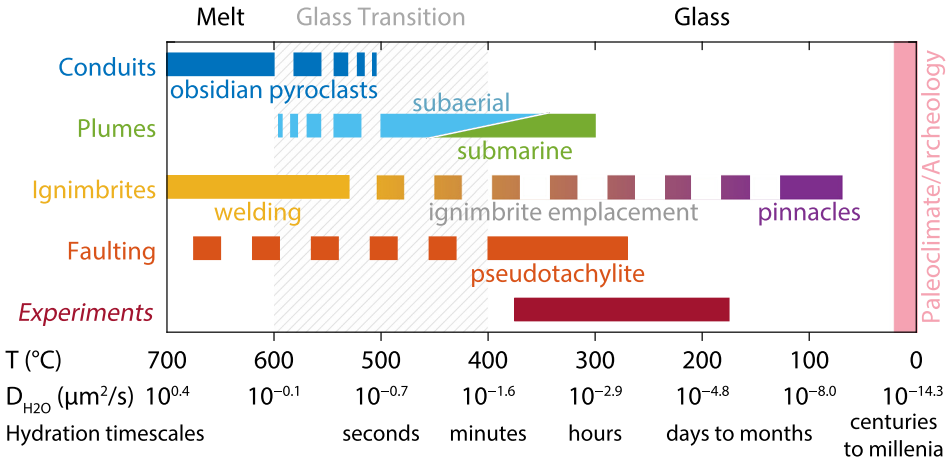

Fig. 1. The temperatures and diffusivities of magma-water or glass-water interactions in various geologic environments. Our experiments between 175 °C and 375 °C overlap with several settings, such as volcanic conduits (Watkins et al., 2012, 2016; Giachetti et al., 2020), eruptive plumes (Hudak et al., 2021; Mitchell et al., 2022), faults (Proctor et al., 2017) and cooling ignimbrites (Gazis et al., 1996; Holt and Taylor, 2001; Hudak and Bindeman, 2018). This work fits into an understudied temperature gap that can disentangle magmatic and secondary source of water in silicic volcanic glasses.

pressures of 0.89–21.1 MPa) relevant to many eruptive products in wet environments such as cooling ignimbrite sheets, submarine pumices, and some subaerial volcanic ash plumes (Randolph-Flagg et al., 2017; Hudak and Bindeman, 2018; Mitchell et al., 2018; Seligman et al., 2018; Rempel and Bindeman, 2019). Three natural rhyolitic volcanic glasses with known δD and major element compositions were used (Table 1). Glass particles >50 μm were air abraded to round them into near spherical oblate ellipsoids. This process involved loading glass into a modified, enclosed ceramic mortar and connecting it to a compressed air hose so the particles would self-abrade (Hudak and Bindeman, 2020). They were then sieved to different size fractions and measured by a particle size analyzer to determine mean particle radii for the size fraction. Rounded, abraded particles with mean radii of 95–160 μm were used for diffusion and mass balance calculations. Glass particles were loaded into Ag capsules suspended over liquid water in stainless-steel vessels, so that the glass would be vapor-hydrated. Experiments were held isothermally and isochorically in a muffle furnace for hours to months (Fig. 2). Enough H_2O (0.36–0.40 mL) was loaded to be an effectively infinite reservoir so that the relative change in H_2O mass in the reservoir, and therefore its δD_{vapor} composition estimated from Horita and Wesolowski (1994) liquid–vapor water fractionation curves, were negligible as H_2O diffused into the glass. For constant temperature and a fixed volume, the proportion of H_2O vapor and liquid H_2O are known and the liquid and vapor δD compositions may be calculated (Figs. 3–5). Experiments listed with multiple durations in Table S1 continued using the same glasses after an aliquot for analysis was removed. The glass particles were dried for ~1 h at 110 °C prior to being reloaded in the vessels with new water following the same initial procedure. For some of the 225 °C and 275 °C experiments, data were generated from glasses hydrated separately in multiple vessels.

Two nominally anhydrous glasses are the same as are described in Hudak and Bindeman (2020): a low silica rhyolite (LSR) from Newberry volcano, Oregon, USA (0.08 wt% H_2O, −100.8‰ δD) and a high silica rhyolite (HSR) from the Summit Lake flow at Yellowstone, Wyoming, USA (0.15 wt% H_2O, −115‰ δD). Discussion in this paper focuses primarily on LSR because H_2O from hydration will quickly swamp residual magmatic H_2O in the glass. Naturally rehydrated high silica perlites from the Nez Perce flow in Yellowstone (~2.90 wt% H_2O, −180.5‰ δD; Bindeman and Lowenstern, 2016) serve to assess D/H exchange between glass and water through time. The hydration water had a δD of +75.6‰ and a $\delta^{18}O$ of +5.9‰ for all experiments with one exception. A series of reverse experiments at 225 °C used isotopically depleted Fairbanks tap water (δD = −152.3‰; $\delta^{18}O$ = −19.2‰) to approach the ΔD_{gl-H2O} from the opposite direction (see Section 2.3). Vapor and liquid δD compositions are calculated using the liquid–vapor fractionations of Horita and Wesolowski (1994) and the expected proportions of liquid and vapor from steam tables (Table S2).

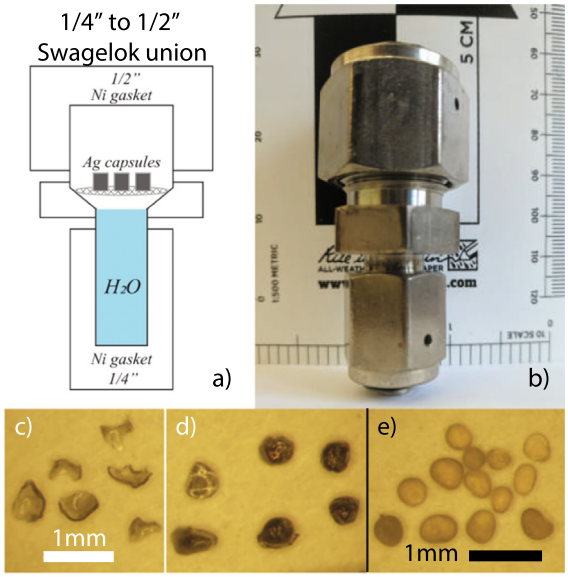

Fig. 2. Schematic (a) and photo (b) of the experimental vessels for glass hydration by water vapor and the experimental materials (c–e). High-Si perlites are separated into skins (c) and cores (d). Note the rims on the cores are likely skins that have not broken off. Abraded LSR particles were sieved to several size fractions including 250–350 μm (e) for experiments. The white and black scale bars correspond to (c, d) and (e), respectively. Modified from Hudak and Bindeman (2020).

2.2. Analytical methods

Simultaneous analyses for H_2O_t and δD_{gl} used milligram quantities of glass and were conducted on a MAT253 isotope ratio mass spectrometer equipped with a high-temperature-conversion, elemental analyzer (TC/EA) at the University of Oregon. Mica standards USGS57 (biotite δD = −91‰), USGS58 (muscovite δD = −28‰), and an internal laboratory standard (biotite, BUD, δD = −151‰) are used for calibration of H_2O_t and δD values and are analyzed 3–5 times throughout each analytical session. Isotope compositions are expressed in delta notation relative to Vienna Standard Mean Ocean Water (VSMOW). Martin et al. (2017) and Bindeman et al. (2021) provided more details about the TC/EA method and established a reproducibility of ±3‰ (2 s.d.) for δD and ±10% for H_2O_t concentrations of ≤1 wt% and ±5% H_2O_t for concentration ≥1 wt% in volcanic glasses. This corresponds to a maximum error of ~0.2 wt% for bulk H_2O measurements by TC/EA. Water concentration maps were made using transmission Fourier transform infrared spectroscopy (FTIR) on a ThermoNicolet iN10-MX at the U.S. Geological Survey in Menlo Park, CA, utilizing an MCT-A detector. Maps were made with aperture-IR spot sizes of 8x8 μm and 20x20 μm for the 225 °C and 375 °C experiments, respectively. We used a default spectral resolution of 8 cm^{-1} and

Table 1
Major element compositions of initial experimental glass as measured by EMPA, previously reported in the Supplementary Data of Bindeman and Lowenstern (2016) and Hudak and Bindeman (2020). The HSR is 08-YS-07 in Loewen et al. (2017) and the perlites are YS-13 in Bindeman and Lowenstern (2016). NBO/T ratios are calculated with normalized major element compositions. Totals reported here do not include Cl, F, or H_2O. Yellowstone glasses use an Fe^{3+}/Fe_{total} of 0.15 for an fO_2 of NNO − 0.7 appropriate for hotspot settings. LSR calculations use an fO_2 of NNO + 0.8 and an Fe^{3+}/Fe_{total} of 0.25 appropriate for arc settings.

Material	Location	No. of analyses		SiO_2 (wt.%)	TiO_2 (wt.%)	Al_2O_3 (wt.%)	FeO_t (wt.%)	MgO (wt.%)	CaO (wt.%)	Na_2O (wt.%)	K_2O (wt.%)	Total (wt.%)	NBO/T
Perlite cores*	Nez Perce flow, Yellowstone, WY, USA	20	Mean	76.02		12.00	0.94	0.01	0.36	3.07	5.55	97.96	0.011
			1σ	0.53		0.10	0.21	0.02	0.11	0.19	0.12	0.62	0.009
Perlite skins*	Nez Perce flow, Yellowstone, WY, USA	20	Mean	73.79		11.67	0.88	0.00	0.33	2.96	5.28	95.16	0.007
			1σ	0.54		0.12	0.21	0.00	0.03	0.11	0.08	0.45	0.005
HSR	Summit Lake flow, Yellowstone, WY, USA	25	Mean	75.11	0.12	12.01	1.19	0.02	0.41	4.13	5.39	98.38	0.035
			1σ	0.51	0.02	0.18	0.10	0.01	0.02	0.22	0.03	0.81	0.004
LSR initial	Newberry volcano, OR, USA	27	Mean	71.45	0.22	14.34	2.03	0.17	0.89	6.95	4.20	100.25	0.070
			1σ	0.72	0.01	0.18	0.15	0.02	0.07	0.38	0.07	0.82	0.008

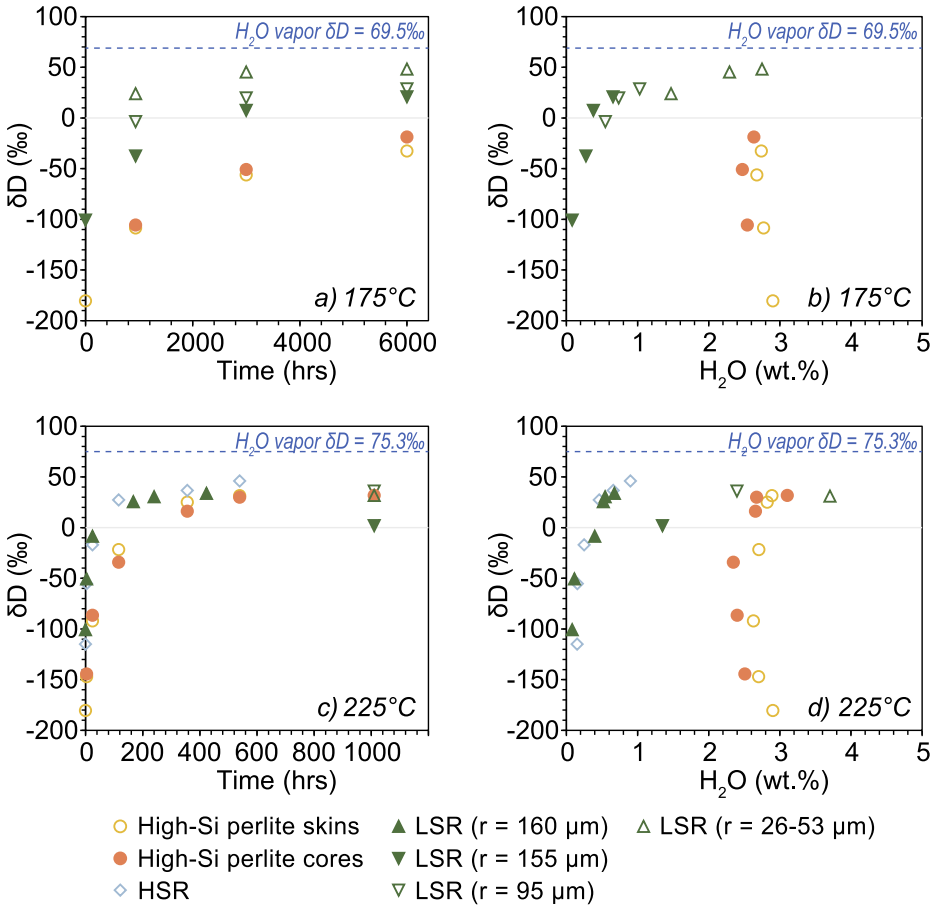

Fig. 3. Bulk δD_{gl} measurements from experiments at 175 °C (a, b) and 225 °C (c, d). Experimental glasses asymptotically approach the δD of the H_2O vapor through time (a, c; dashed line). Nominally anhydrous glasses increase in H_2O with time while perlites dehydrate by no >0.2 wt% before recovering to higher H_2O (b, d). Vapor δD composition is computed based on the initial water δD values and fractionation factor from Horita and Wesolowski (1994).

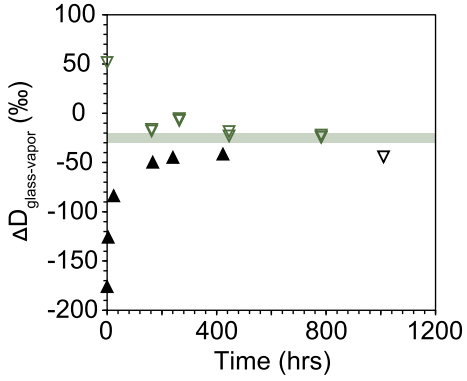

Fig. 4. Results from the 225 °C experiments from Fig. 3c-d are shown in black and compared to results from a set of reverse experiments (green) using the 26–53 μm radii unabraded LSR particles and Fairbanks H_2O (δD = −152.3‰). A shaded green box shows $\Delta D_{gl\text{-}H2O}$ of −25 ± 5‰, corresponding to the preferred models in Fig. 12.

other defaults discussed in Lowenstern and Pitcher (2013). Water concentrations were quantified by means of the near IR peaks at 4500 and 5210 cm^{-1} using the method of Zhang et al. (1997). Secondary electron images of the surfaces of the glasses were taken using a FEI Quanta 200 ESEM/VPSEM microscope at 2.0 keV and 10 Pa. Energy dispersive X-ray spectroscopy (EDX) for the major element chemistry of the glass surface and secondary phases on the glass surface was conducted on an Thermo Scientific Apreo 2 Scanning Electron Microscope at 15.0 keV and 3.2 nA. The EDX data are semi-quantitative and may have significant errors, especially for H_2O-by-difference estimates, which are taken by subtracting the total from 100 wt%.

2.3. Isotope notation

Analytical results are presented in delta notation:

$$\delta D_{gl}(‰) = 1000\left(R^{D/H}_{glass}/R^{D/H}_{VSMOW} - 1\right), \quad (1)$$

where $R^{D/H}_{VSMOW}$ = 1/6420 is the isotopic ratio of the standard. Equilibrium isotope partitioning between glass and fluid phases is given as:

$$\alpha^{D/H}_{gl\text{-}H2O} = R^{D/H}_{gl}/R^{D/H}_{vapor} = \frac{1000 + \delta D_{gl}}{1000 + \delta D_{vapor}}. \quad (2)$$

Values for $\alpha_{gl\text{-}H2O}$ are generally close to 1.000 and can be more directly compared to the compositions of the two phases in units of ‰ using the expression, $10^3 \ln\alpha_{gl\text{-}H2O}$. However, this term implies isotopic equilibrium between glass and vapor, so $10^3 \ln\alpha_{gl\text{-}H2O}$ is reserved for modeling of the equilibrium H isotope fractionation between glass and water vapor and where we explicitly interpret equilibrium fractionation. Throughout most of the text, direct comparison of the δD_{gl} results to the δD_{vapor} uses ΔD notation, which is agnostic with respect to equilibrium and kinetic isotope effects. Here,

$$\Delta D_{gl\text{-}H2O} = \delta D_{gl} - \delta D_{vapor}. \quad (3)$$

This can be calculated for any individual δD result.

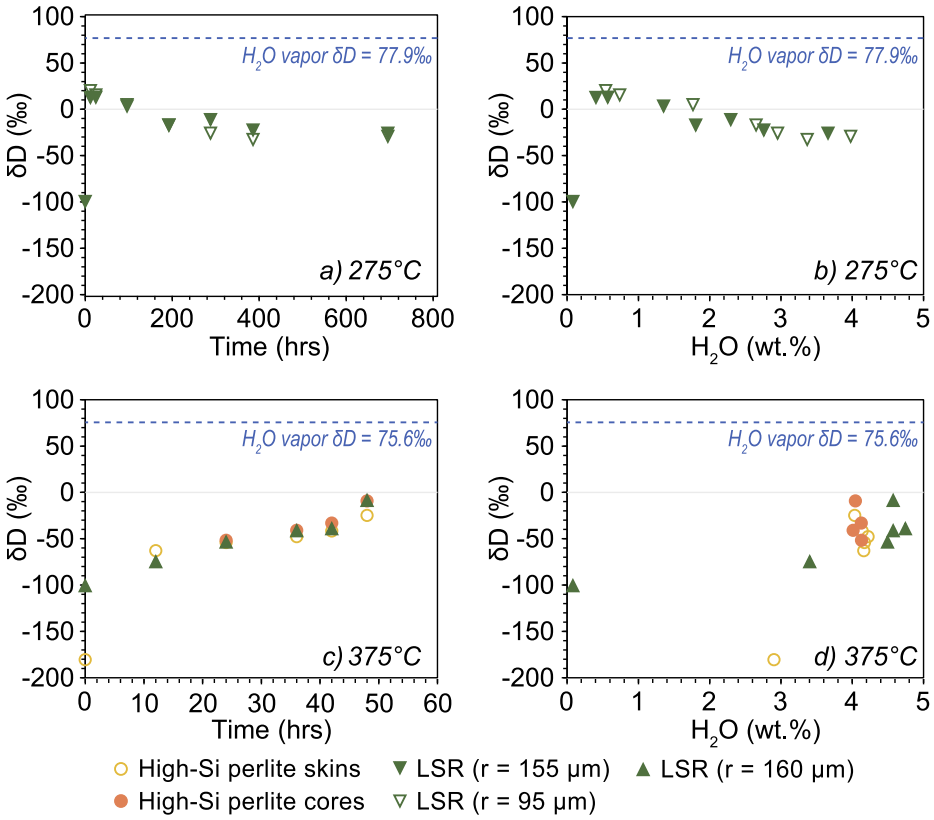

Fig. 5. Bulk δD_{gl} measurements from experiments at 275 °C (a, b) and 375 °C (c, d). Experimental glasses never exceed + 20‰ δD_{gl} and remain isotopically light relative to δD_{vapor} (dashed line). At 275 °C, the glass increases dramatically in the shortest duration experiment before decreasing (a), which differs from the 375 °C trend that increases through time (c). Linear increases in H_2O through time at 275 °C cause the H_2O trend to mirror the time series (b), which again differs from the 375 °C glasses that rapidly reach their H_2O solubility and slowly increase in δD.

3. Analytical results

3.1. TC/EA δD results

Experimental glasses hydrated with heavy water vapor (minimum of +69.5‰) increased monotonically in δD_{gl} through time from their initial hydrogen isotope compositions (<−100‰), with the notable exception of the 275 °C experiments. A reverse experiment at 225 °C with isotopically negative Fairbanks water (−152.3‰) produced a monotonically decreasing trend of $\Delta D_{gl\text{-}H2O}$ similar to the heavy water vapor experiments. In the experiments at 175 °C and 225 °C, δD_{gl} attained positive values, whereas in experiments at 275 °C and 375 °C δD_{gl} remained strongly negative (Figs. 3–5). Based on these contrasting observations, we separate the results into two regimes: below 250 °C and above 250 °C.

3.1.1. Equilibrium fractionation below 250 °C results

In experiments below 250 °C, the δD_{gl} steadily increased to high positive δD_{gl} values (Fig. 3). In LSR, the δD_{gl} monotonically increased with the greatest increases occurring over during the initial hydration, which produced asymptotic curves. This trend is apparent in all LSR particle sizes (Fig. 3a) in the 175 °C experiments. The largest size fraction (r_{eff} = 155 μm, rounded) increased most slowly in δD towards the vapor composition of +69.5‰. The intermediate particle size (r_{eff} = 95 μm, rounded) increased in H_2O and δD_{gl} at a rate between the larger and smaller particle sizes and achieved a maximum δD_{gl} of 27.6‰. The smallest particle size (r_{eff} = 26–53 μm, angular) yielded the highest δD_{gl} values of +45.3‰ and +48.3‰ after 3000 and 6000 h, respectively (Table 2). The δD_{gl} between these two experiments effectively remained unchanged even though the experimental duration was doubled and an additional ~0.5 wt% H_2O diffused into the glass, reaching 2.75 wt% (Fig. 3b). The mean difference between δD_{gl} and δD_{vapor} gives a $\Delta D_{gl\text{-}H2O}$ of −22.7‰. Similarly, LSR particles asymptotically approached a plateau in δD_{gl} at 225 °C (Fig. 3c; Table 2). The LSR glasses hydrated for at least 240 h (>0.5 wt% H_2O), with just one exception, and converged on a mean δD_{gl} value of 32.6‰ regardless of particle size (n = 4, 4.3‰ 2σ). This mean δD_{gl} corresponds to a $\Delta D_{gl\text{-}H2O}$ of −42.7‰ at 225 °C. The HSR achieved a notably higher maximum δD_{gl} value of +46.0‰, corresponding to an $\Delta D_{gl\text{-}H2O}$ of −29.3‰. The H_2O-δD_{gl} evolution at 225 °C (Fig. 3d) followed a similar trajectory as the glasses in the 175 °C experiments (Fig. 3b). The δD_{gl} of the nominally anhydrous glasses increased rapidly at low H_2O and then plateaued above 1 wt%.

The perlites also increased asymptotically in δD_{gl} through time below 250 °C. Because the perlites initially contained nearly 3 wt% of preexisting meteoric H_2O with a δD of −180‰, the experimental water added could not as quickly overprint the initial δD_{gl} values by diffusive exchange of H_2O within and outside of the glass. This resulted in a slower, but nonetheless monotonic increase toward the equilibrium $\alpha_{gl\text{-}H2O}$ value (Fig. 3a). At 175 °C, neither the perlite skins nor cores ever achieved positive δD_{gl}. Even in the 6000-hour-long experiments the maximum observed δD_{gl} was −18.8‰ (Table 2). However, at 225 °C, perlite skins and cores attained δD_{gl} comparable to the LSR δD_{gl}, yielding an $\Delta D_{gl\text{-}H2O}$ of −43.6‰. We observe that perlites initially dehydrated with the earliest increases in δD_{gl} (Fig. 3b, d) in both of these sets of experiments. While the 175 °C perlites never fully recovered their initial H_2O

Table 2
Total H_2O and δD data for experimental glasses. Errors for δD are < 3‰ (1σ, n = 3–5) for standards USGS57 and USGS58. Italicized H_2O_t concentrations are from Hudak and Bindeman (2020). See Table S2 for vapor δD compositions.

Material	Effective radius (μm)	Duration (hours)	H_2O (wt.%)	δD (‰)	$\Delta_{g\text{-}v}$ (‰)
Initial Experimental Glass Compositions					
LSR	n/a	0	*0.08*	−100.8	
HSR	n/a	0	*0.15*	−115.0	
Perlite skins	n/a	0	*2.90*	−180.5	
175 °C Experimental Results					
LSR	155	935	*0.28*	−37.6	
LSR	155	3000	*0.38*	7.5	
LSR	155	6000	*0.65*	20.9	−48.6
LSR	95	935	*0.55*	−4.8	
LSR	95	3000	*0.74*	18.7	
LSR	95	6000	*1.03*	27.6	−41.9
LSR	26–53[a]	935	*1.47*	23.9	
LSR	26–53[a]	3000	*2.29*	45.3	−24.2
LSR	26–53[a]	6000	*2.75*	48.3	−21.2
Perlite skins	n/a	935	*2.77*	−108.5	
Perlite skins	n/a	3000	*2.68*	−56.3	
Perlite skins	n/a	6000	*2.74*	−32.7	
Perlite cores	n/a	935	*2.54*	−105.6	
Perlite cores	n/a	3000	*2.47*	−50.9	
Perlite cores	n/a	6000	*2.64*	−18.8	
225 °C Experimental Results					
LSR	160	4	*0.20*	−50.6	
LSR	160	24	*0.40*	−8.5	
LSR	160	167	*0.52*	25.6	
LSR	160	240	*0.54*	30.4	−44.9
LSR	160	423	*0.67*	33.8	−41.5
LSR	155	1010	*1.35*	2.0	
LSR	95	1010	*2.40*	35.0	−40.3
LSR	26–53[a]	1010	*3.70*	31.2	−44.1
HSR	n/a	4	*0.15*	−55.2	
HSR	n/a	24	*0.25*	−17.0	
HSR	n/a	116	*0.46*	27.4	
HSR	n/a	356	*0.66*	36.8	
HSR	n/a	539	*0.90*	46.0	−29.3
Perlite skins	n/a	4	*2.70*	−147.1	
Perlite skins	n/a	24	*2.63*	−92.1	
Perlite skins	n/a	116	*2.71*	−21.5	
Perlite skins	n/a	356	*2.82*	25.0	
Perlite skins	n/a	539	*2.89*	31.6	−43.7
Perlite cores	n/a	4	*2.51*	−144.3	
Perlite cores	n/a	24	*2.40*	−86.4	
Perlite cores	n/a	116	*2.34*	−34.2	
Perlite cores	n/a	356	*2.66*	16.1	
Perlite cores	n/a	539	*2.67*	30.0	
Perlite cores	n/a	1010	*3.10*	31.8	−43.5
225 °C Reverse[i] Experimental Results					
LSR	26–53[a]	162.92	*1.90*	−168.6	
LSR	26–53[a]	162.92	*1.88*	−170.2	
LSR	26–53[a]	263.75	*2.90*	−157.8	
LSR	26–53[a]	263.75	*2.91*	−159.1	
LSR	26–53[a]	263.75	2.82	−159.5	
LSR	26–53[a]	445.52	2.17	−170.9	
LSR	26–53[a]	445.52	*2.18*	−175.3	
LSR	26–53[a]	781.97	*3.46*	−176.3	−24.0
LSR	26–53[a]	781.97	*3.26*	−174.4	−22.1
LSR	26–53[a]	781.97	*3.42*	−176.5	−24.2
275 °C Experimental Results					
LSR	155	12	*0.40*	11.5	
LSR	155	24	*0.57*	11.8	
LSR	155	96	*1.35*	2.3	
LSR	155	192	*1.80*	−18.3	
LSR	155	288	2.29	−12.4	
LSR	155	386	2.76	−23.6	−101.5
LSR	155	696	3.66	−27.1	−105.0
LSR	95	12	*0.54*	18.9	
LSR	95	24	*0.74*	14.3	
LSR	95	96	*1.77*	3.7	
LSR	95	192	*2.65*	−18.3	

Table 2 (*continued*)

Material	Effective radius (μm)	Duration (hours)	H_2O (wt.%)	δD (‰)	$\Delta_{g\text{-}v}$ (‰)
LSR	95	288	2.95	−27.0	−104.9
LSR	95	386	3.37	−33.7	−111.6
LSR	95	696	3.98	−30.4	−108.3
375 °C Experimental Results					
LSR	160	12	*3.40*	−74.9	
LSR	160	24	*4.50*	−53.5	
LSR	160	36	*4.57*	−41.3	
LSR	160	42	*4.75*	−39.1	
LSR	160	48	*4.57*	−8.7	−84.4
Perlite skins	n/a	12	*4.16*	−62.8	
Perlite skins	n/a	24	*4.17*	−54.0	
Perlite skins	n/a	36	*4.22*	−47.8	
Perlite skins	n/a	42	*4.14*	−41.7	
Perlite skins	n/a	48	*4.03*	−24.8	−100.5
Perlite cores	n/a	24	*4.13*	−51.7	
Perlite cores	n/a	36	*4.02*	−41.0	
Perlite cores	n/a	42	*4.12*	−33.0	
Perlite cores	n/a	48	*4.04*	−9.1	−84.8

[a] The smallest, non-abraded particle sizes could not be measured, so the range of radii given is half of the sieve fraction (53–105 μm) for these particles.
[†] Reverse experiments use Fairbanks H_2O with a δD of −152.3‰.

concentration of 2.9 wt% (in the skins), the perlites at 225 °C eventually increased to 3.1 wt% H_2O as their δD_{gl} approached the plateau of +31.7‰. This dehydration was minimal, never registering >0.3 wt% decrease from the initial H_2O. The perlites at 225 °C eventually recovered their initial H_2O content and reached a maximum of 3.1 wt% H_2O after 1010 h of hydration.

An additional set of reverse experiments was conducted at 225 °C with Fairbanks tap water (δD = −152.3‰) and the smallest set of angular, non-abraded LSR glass particles. At the longest duration, 782 h, δD_{gl} reached −175.7‰ corresponding to a $\Delta D_{gl\text{-}H2O}$ of −23.4‰ (green; Fig. 4). For comparison, the other set of experiments (black symbols) obtain a $\Delta D_{gl\text{-}H2O}$ of −42.7‰. This ~20‰ gap in $\Delta D_{gl\text{-}H2O}$ suggests that LSR is approaching but has not reached isotopic equilibrium in either set of experiments.

3.1.2. Kinetic isotope effects above 250 °C results

The higher temperature glasses acquired much lower δD_{gl} values than those in experiments below 250 °C despite gaining more H_2O (Fig. 5). The time series of δD_{gl} at 275 °C is the most enigmatic of all the experiments. After just 12 h, both LSR glass particle sizes (r_{eff} of 95 μm and 155 μm) increased by >110‰, plateaued at 24 h, and decreased thereafter until the end of the experiment at 696 h (Fig. 5a). This trend was mirrored in the H_2O-δD_{gl} evolution of LSR, where H_2O steadily increased to 3.7 and 4.0 wt% while δD_{gl} decreased to −27.1‰ and −30.4‰ for particles with 155 μm and 95 μm radii, respectively (Fig. 5b). The minimum δD_{gl} of −33.7‰ in these experiments was achieved after 386 h in the intermediate particle size (r_{eff} = 95 μm). For the 275 °C experiments, δD_{gl} may have plateaued between −23‰ and −34‰ with a mean of −28.1‰ (n = 3) in samples with ≥ 3 wt% H_2O (Fig. 5a-b). These results yield a $\Delta D_{gl\text{-}H2O}$ of −106‰ at 275 °C. If a similar initial increase in δD_{gl} occurred in the 375 °C experiments, the temporal sampling resolution was not fine enough to capture it. The δD_{gl} of LSR particles (r_{eff} = 95 μm) increased for each duration (Fig. 5c), even as H_2O plateaued after 24 h (Fig. 5d). Even after just 12 h at 375 °C, the LSR glass had 3.40 wt% H_2O. Through 42 h, the δD_{gl} composition reached a plateau before increasing again to a δD_{gl} of −8.7‰ after 48 h.

Perlites followed a very similar time-δD_{gl} evolution to the 160 μm LSR particles despite their large initial differences in both H_2O and δD_{gl} (Fig. 5c). Even the abrupt increase in δD_{gl} between 42 and 48 h was not limited to the LSR glass. The perlite cores increased to −9.1‰ δD_{gl} while the skins increased less dramatically to −24.8‰ at 48 h. The result for the cores was effectively identical to that of the LSR with a $\Delta D_{gl\text{-}H2O}$ of −84.8‰. The perlite skins and cores plateaued in H_2O prior to 12 h even as δD_{gl} continued to slowly increase (Fig. 5d). All measured H_2O results were nearly identical with 4.12 ± 0.11 wt% H_2O, within analytical precision of the TC/EA for high H_2O samples (Martin et al., 2017).

3.2. FTIR results

The distribution of water and its species in a glass can be determined using FTIR spectroscopy. Mid-IR spectra of an LSR particle from a 240-hour-long and a 423-hour-long experiment at 225 °C showed no apparent increase in OH^- with the addition of H_2O_m to glass during rehydration (Fig. S1). Measurements taken from the interior of the glass particles, which have not been affected by secondary hydration, show approximately 0.1 wt% initial magmatic H_2O_t at the 3500 cm^{-1} peak and effectively no H_2O_m at the 1600 cm^{-1} peak. The ~0.1 wt% H_2O can be attributed entirely to OH^-, consistent with the 1 atm solubility of water in obsidian. The rim of the glass shows no apparent change to the OH^- concentration, but an addition of 0.4–0.5 wt% H_2O_m at the 1600 cm^{-1} peak for both the 240 and 423 h-long durations for H_2O_t of 0.5–0.6 wt% at the 3500 cm^{-1} peak (Fig. 6; Fig. A1). After 48 h at 375 °C and

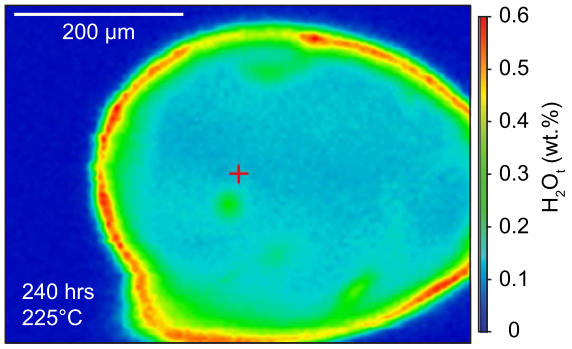

Fig. 6. FTIR map of H_2O_t in a glass particle from the 240 h-long experiment at 225 °C. The length scales of hydration are consistent with the profile measured by NanoSIMS in Hudak and Bindeman (2020). Water concentrations get lower towards the edges as they thin from the full thickness of the doubly polished wafer.

21 MPa, LSR obsidian is fully hydrated and has begun to repartition H_2O_m into OH^-. Both the 1600 cm^{-1} and the 3500 cm^{-1} peaks in thin glass wafers are oversaturated in IR spectra, so the near-IR peaks were used to determine H_2O_m and OH^-. The near-IR 5200 cm^{-1} peak and the 4500 cm^{-1} peak indicate that there is approximately 5.9 wt% H_2O_m and 1.0 wt% OH^-, respectively (Fig. 7). Attenuated total reflectance (ATR) FTIR (Lowenstern and Pitcher, 2013) spectra confirmed that the glass contained a homogeneous 6.9 wt% H_2O_t.

3.3. Glass surface textures and chemistry

We examined changes on the glass surface with high resolution SEM images and EDX composition for LSR experiments at each temperature. Lower temperature (<250 °C) experiments demonstrated minimal changes in composition, consistent with observations and microprobe data showing that the glass interior remained unaltered (Hudak and Bindeman, 2020). Below 250 °C, ≤2 μm thick coating of altered glass and alterations products are present on the surface of the glass (Fig. 8a). Isolated aggregates or individual crystals nucleated on the glass surface and seldom exceeded 4 μm in diameter. The sole exception to this is the longest duration 225 °C experiments (1010 h), and experiments above 250 °C glass had pervasive surface alteration where rare isolated cubic phases of up to 15 μm in width occur on the surface of the LSR particles (Fig. 8b). Finer grained (<4 μm) rhombohedral and/or elongated pyramids and radiating pyramidal aggregates coat these long duration LSR particles (Fig. 8c).

Above 250 °C, both secondary alteration and glass dissolution textures are observed (Fig. 9). Secondary phases form a more continuous matrix coating on glass surfaces in the 275 °C experiments than in the 375 °C experiments. While these coatings of alteration products are thicker (Fig. 9a) and/or more interconnected (Fig. 9b), they also maintain a sharp boundary with unaltered glass from which they readily detach, which may explain why glass chemistry in the interior of polished grains show no significant variation between rims and cores (Hudak and Bindeman, 2020). Secondary electron images show a matrix coating generally not exceeding 5 μm of other finer grained alteration products at 275 °C, with cubic phases embedded within some experiments (for example, after 192 h, but not after 386 h; Fig. 9a–c). Localized dissolution textures are much more prevalent on LSR particles from the above 250 °C experiments and may be restricted to these conditions. These include pitted, scalloped glass surfaces visible where the alteration layer has cleanly separated and gaps along the interface

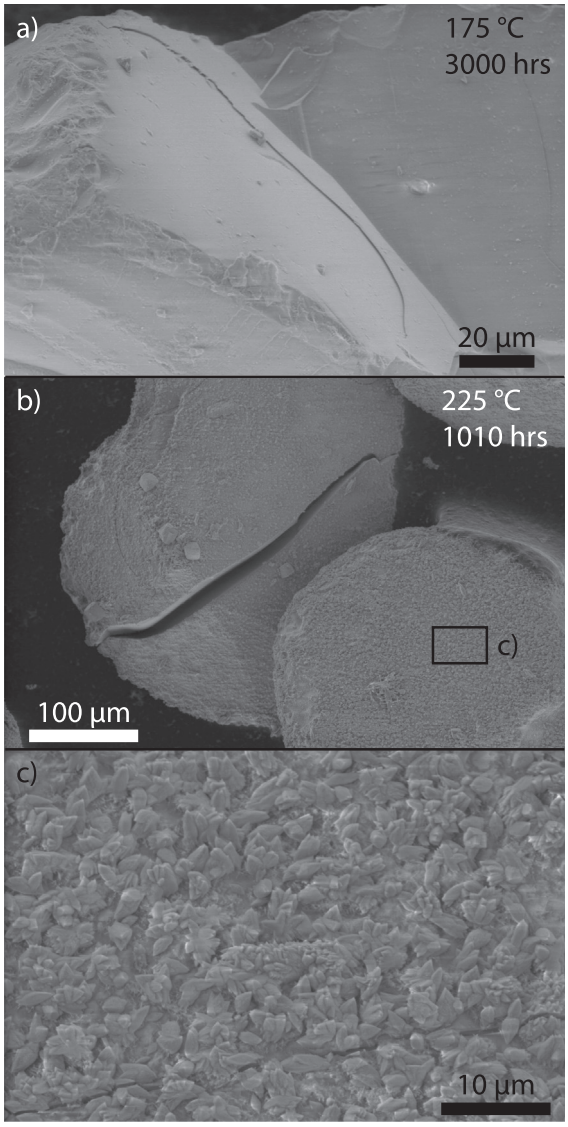

Fig. 8. Secondary phases sparce on the surface of the 175 °C glasses, but a thin layer in the 3000 h-long experiment can be seen chipping off the surface (a). Secondary phases are also uncommon in the shorter duration 225 °C, but after 1010 h, some cubic phases up to 15 μm across are present (b) along with a thin layer of pyramidal or polyhedral aggregates (c).

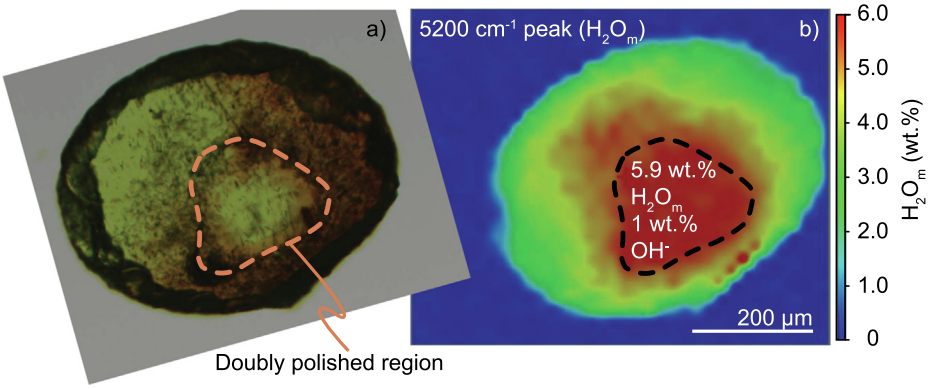

Fig. 7. An optical image (a) and an FTIR map of H_2O_m in a glass particle from the 48 h-long experiment at 375 °C (b). The dashed line shows where the wafer is doubly polished to a consistent thickness with H_2O_m and OH^- formed during hydration. Outside of this area, the glass tapers and becomes thinner and therefore yields lower H_2O_m concentrations.

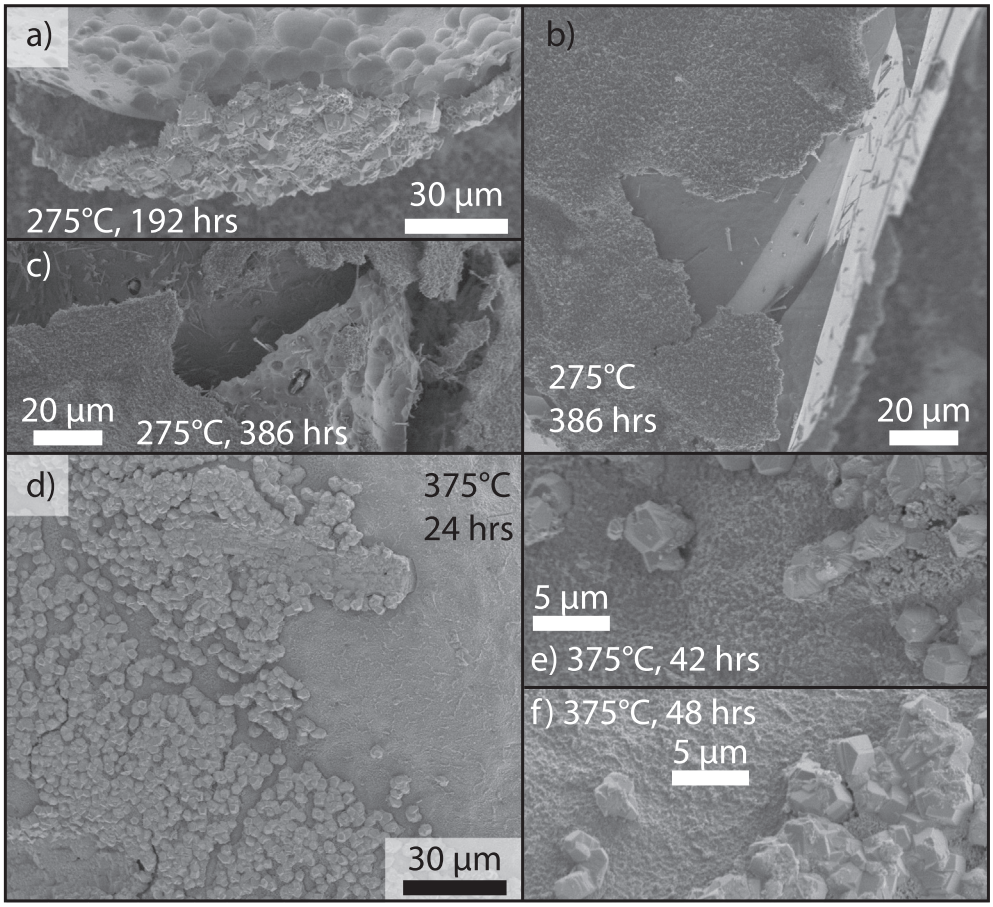

Fig. 9. Secondary electron images of two particles of LSR glass at 275 °C (a–c) and 375 °C (d–f). The 192 h-long experiment has the thickest coating of alteration products of any experiment at any temperature (a). The layer up to 4–5 µm in thickness with isolated cubic phases up to 10 µm across. A longer duration experiment (b–c; 386 h) has a surface coating of secondary phases uniform in thickness (<4 µm). Exposed glass surfaces are not uniform in appearance as some areas have smooth, flat surfaces (b) while others are pitted (c). Dissolution textures in (c) include pitting along the glass-plagioclase microlites interface (f). At 375 °C for 24 h (d), 42 h (e), 48 h (f), the main, polyhedral secondary phase on the glass surface remains unchanged in composition (Fig. 10 and Table S3), appearance, or size after 24 h (d–e).

between plagioclase microlites and the glass (Fig. 9c). Experiments at 375 °C have more developed cubic to polyhedral secondary phases 2–5 µm in diameter (Fig. 9d–f). They occur both isolated and in continuous, interconnected patches (Fig. 9d). Regardless of experimental duration – 24, 42, or 48 h – the population remains relatively unchanged.

Semi-quantitative EDX analyses are used to identify the possible phases forming on the glass surface. These data include spots directly on glass as well as secondary phases grown on the glass surface, both as single crystals and as a matrix layer. Data from all experimental durations are plotted together by temperature (Fig. 10). Most secondary phases and alteration rinds are thin enough (<3 µm) that some underlying glass is likely to be included in the activation volume during EDX analysis. Additionally, this analytical volume likely includes a gel layer and glass that has lost mobile cations but has not yet been altered to secondary phases. The raw concentrations (Table S3) show no depletion in Al_2O_3 below (Fig. 10a) or above 250 °C (Fig. 10b) for any experimental duration compared to the initial LSR glass composition. This is not consistent with zeolite phases (triangles; Fig. 10) that are commonly lower in both Al_2O_3 and SiO_2 than the initial rhyolitic glass (LSR) composition. Iron enrichments are rare, but notable where they occur (Fig. 10c–d). Nearly all analyses in all experiments record depletions in Na_2O occur on the glass surfaces (Fig. 10e–f). At all temperatures, the glass is slightly depleted in K_2O, but some phases have strong enrichments of up to 12 wt% (Fig. 10g–h). Clear populations of K_2O enrichment occur in the fine-grained matrix of secondary phases coating the surface of the glasses in the 275 °C experiments and the polyhedral phases that coat the glass surface in the 375 °C experiments (Fig. 10; Table S3). Water-by-difference is determined by subtracting the oxide total in wt% from 100 and assumes the rest of the material consists of H_2O. Water-by-difference estimates form an array that fits the curve defining simple dilution of glass SiO_2 concentration as H_2O is added (Fig. 10i–j). Slight enrichments in SiO_2 relative to the curve can be attributed to the loss of Na from the glass. Potential mineral candidates are plotted in Fig. 10. It is likely that zeolites, phyllosilicates, and other alteration minerals comprise a diverse assemblage within these layers and that alteration paragenesis may cause changes through time at the glass surface.

Volumetrically, however, alteration phases do not dominate the H_2O or δD budget of the analyzed bulk materials using mass balance approaches. Quantitative microprobe work from a previous study on the internal chemistry of bisected glass particles from these experiments confirms that even the outer 5 µm of the glass are chemically unchanged beyond the addition of H_2O (Hudak and Bindeman, 2020). No alteration is observed within the glass particles down to the resolution of Quanta EXS (40 nm). Alteration occurs only on the surface of glass particles and these alteration layers are discontinuous. Therefore, the majority of the material remains fresh glass volumetrically (>91% even for a continuous 3 µm layer on the medium sized particles). Thus, it is hydrated glass that dominates the H_2O budget, and the hydrogen isotope composition, of measured bulk material. The primary influence of

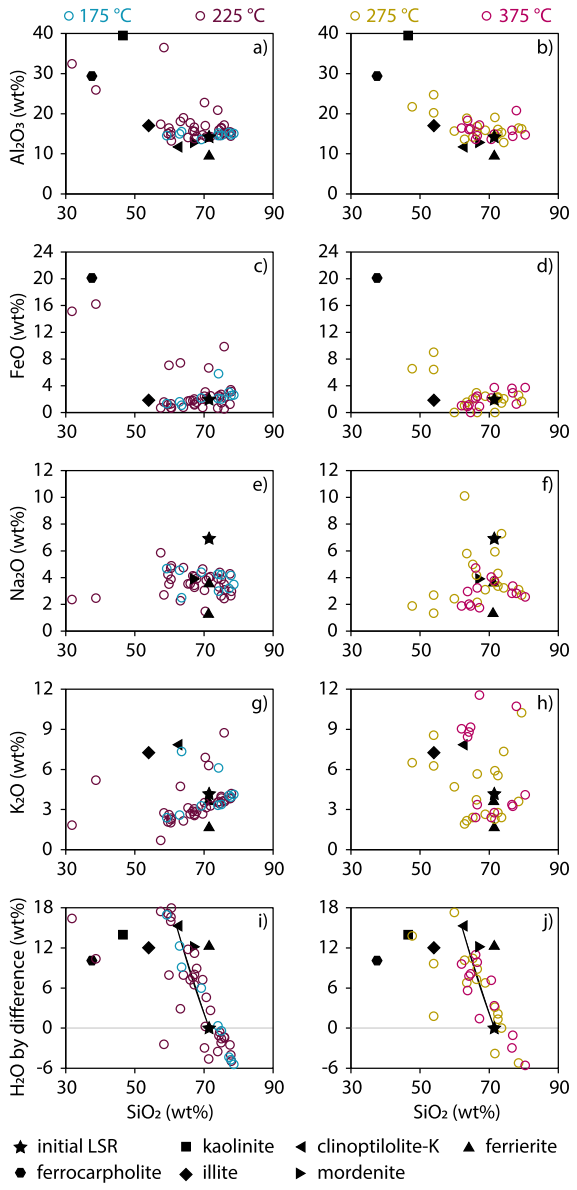

Fig. 10. Plots of EDX data from the glass surfaces and secondary phases are shown for SiO_2 vs Al_2O_3 (a–b), FeO (c–d), Na_2O (e–f), K_2O (g–h), and H_2O by difference (i–j). Data are plotted by experimental temperatures and include all durations. Results from 175 °C and 225 °C are plotted on the left and 275 °C and 375 °C are plotted on the right.

secondary phases could instead be related to changes to the δD boundary conditions of H_2O diffusing into the glass, which we discuss in Section 4.2.

4. Discussion

Experiments below and above 250 °C produce divergent results: lower temperature LSR glasses and perlites approach raw $\Delta D_{gl\text{-}H2O}$ values within the range of −33 ± 11‰, while higher temperature experiments yield highly negative δD_{gl} values and raw $\Delta D_{gl\text{-}H2O}$ values of ≤−85‰. A set of reverse experiments at 225 °C (Fig. 4) produces $\Delta D_{gl\text{-}H2O}$ within the given range but remains offset from the other 225 °C $\Delta D_{gl\text{-}H2O}$ results by about 20‰. This suggests equilibrium has not been achieved in either experiment but are converging on an equilibrium fractionation factor that can be modeled using diffusion-mass balance approaches. The FTIR data from 375 °C indicates repartitioning of H_2O_m to OH^- and SEM images showing surficial glass alteration, particularly above 250 °C, provide two mechanisms by which kinetic isotope effects may dominate relative to equilibrium partitioning between glass and vapor could be inhibited.

4.1. Glass surface changes and secondary phases

Glass is a metastable amorphous phase that begins to decompose into crystalline phases when exposed to fluids at elevated temperatures for long durations. Much of the literature devoted to the use of glass for long-term nuclear storage focuses on glass stability and alteration with liquid H_2O at temperatures of <100 °C characteristic of buried disposed waste (Gin et al., 2021), although many glasses decompose even in the presence of water vapor at low temperatures and relative humidity (Majérus et al., 2020, and references therein). Our work and the work of others have determined that the glass hydration and alteration occurs in 3 main stages: (1) glass hydration by H_2O_m, (2) exchange of H+ with fluid mobile cations in the glass structure (Cerling et al., 1985; Oelkers, 2001; Gin et al., 2015; Hellmann et al., 2015; Hudak and Bindeman, 2020), and (3) hydrolysis reactions that break Si—O—X bonds and leach out alkalis (Cerling et al., 1985) and form secondary phases. Through this last step, the solid glass phase is finally destroyed (Oelkers, 2001; Declercq et al., 2013). This set of processes results in a complex set of layers between the external fluid and unaffected, pristine glass (Gin et al., 2015; Hellmann et al., 2015; Cassel and Breecker, 2017). Secondary phases such as Na and Ca-rich zeolites, most commonly analcime (Fournier et al., 2014, and references therein), form on the surface (Bates and Steindler, 1982; Bates et al., 1982; Bakel et al., 1995; Neeway et al., 2012; Fournier et al., 2017). Immediately below this crystalline layer, a passivating gel layer may develop and densify as silica tetrahedra polymerize with the loss of cations (Jollivet et al., 2008; Gin et al., 2015, 2018). This eliminates much of the porosity in the gel, preventing the diffusion of H_2O into the glass and greatly slowing glass alteration. However, both zeolite growth and vapor hydration facilitate additional glass alteration and hydration (Bates and Steindler, 1982; Fournier et al., 2014, 2017).

However, enrichments of Na and Ca are notably absent in the EDX data of glass surface and alteration products (Fig. 10; Table S3). We searched for other zeolites that have been documented as alteration phases in naturally and experimentally altered rhyolitic tuffs at high temperatures, such as mordenite (Randolph-Flagg et al., 2017), ferrierite (Cullen et al., 2019), and clinoptilolite. Each of these phases are consistent with some, but not all, of the EDX major element data including SiO_2, Al_2O_3, and the alkalis to some extent. The phases or aggregates of multiple phase that are enriched in FeO and Al_2O_3 are most consistent with a phase called ferrocarpholite, although it is also possible that nanolites of iron oxides and kaolinite (<40 nm) coexist on the glass surface. The EDX data are not consistent with a thick, well-developed Si-rich passivating gel layer, which may not be expected in vapor hydration experiments depending on the glass chemistry (Fournier et al., 2014). Therefore, we assume diffusion of H_2O_m into the glass continues unimpeded. We observe a strong negative correlation between SiO_2 and H_2O-by-difference (Fig. 10i–j) suggestive of a thin, H_2O-rich altered glass layer. The chemical and mineralogical changes on the glass surface, especially present in the higher temperature experiments, can affect the isotopic composition of the H_2O that diffuses into the glass.

4.2. Surface effects on bulk H_2O and δD

Glass surface alteration will affect the bulk H_2O and δD_{gl} composition and affect the δD at the boundary. The extent to which

the alteration layer contributes to the bulk H_2O measurements depends on: (1) the isotopic fractionation at the boundary, and (2) the relative proportions of the alteration thickness and the penetration depth of H_2O diffusion into glass. As previously discussed in Section 3.4, the bulk of the experimental materials remains fresh glass and with alteration confined to the glass surfaces, and primarily on the glasses from experiments above 250 °C.

While a surface coating of zeolites or phyllosilicates has the potential to contribute a considerable amount of H_2O to bulk H_2O measurement, SEM imaging indicates that these phases are not volumetrically substantial in our lower temperature, short duration experiments. The low initial and measured H_2O concentrations of LSR particles make their H_2O contents susceptible to even small amounts of zeolites on the surface. However, the maximum bulk H_2O in 225 °C experimental results <1010 h is only 0.67 wt%. NanoSIMS measurements of H_2O diffusion profiles in a 334 h-long experiment at 225 °C have a half-fall distance of 9 μm corresponding to 0.37 wt% H_2O in the bulk glass (Hudak and Bindeman, 2020) that do not require additional sources of H_2O from hydrous secondary phases. We argue that glass alteration is primarily limited to the first two stages (hydration and cation loss) below 250 °C in our vapor hydration experiments.

With more extensive hydration, in the absence of hydrous phase growth, the glass contribution to the bulk H_2O and δD_{gl} should increase. The 375 °C experiments are a good example as there is no change in the composition, appearance, or size of the secondary phases between 24 and 48 h, over which time the glass becomes completely hydrated into the interior up to 6.9 wt% (Fig. 7). In this case, using a conservative estimate of a continuous 3 μm layer of alteration products with 15 wt% H_2O, hydrated glass still contributes >94% of the bulk H_2O and should dominate the measured bulk δD_{gl} composition. Notably, it is in these experiments that extremely large $\Delta D_{gl\text{-}H2O}$ is obtained, indicating that either the boundary or a reaction internal to the glass is the primary cause of the observed isotopic fractionation.

Equilibrium and kinetic isotope effects associated with a complex boundary layer are all difficult to incorporate into a model without contrived assumptions. Assessing the mineralogical changes on the isotopic boundary condition for H_2O diffusion is complicated in part by the uncertainty of D/H fractionation between common glass alteration products, zeolites and phyllosilicates, and H_2O. There are no well-constrained hydrogen isotope fractionations for zeolites (Karlsson and Clayton, 1990). This water-rich family can incorporate H_2O into its structure and into cavities within the framework silicate structure, which likely have site specific partitioning of H isotopes. Channel waters in analcime have δD values that correlate with latitude and that loosely plot along the meteoric water with their channel water $\delta^{18}O$ (Karlsson and Clayton, 1990). Phyllosilicates, though better constrained, also have complex D/H fractionations with a coexisting fluid phase. Within our experimental temperature window, the $1/T–10^3\ln\alpha_{min\text{-}H2O}$ relationships for hydrous minerals are diverse. In addition, D/H fractionations between kaolinite and H_2O may increase dramatically (Vennemann and O'Neil, 1996), subtly increase (Sheppard and Gilg, 1996; Méheut et al., 2010), or decrease with decreasing temperature (Lambert and Epstein, 1980). For example, experimentally determined $10^3\ln\alpha$ relationships for kaolinite-H_2O yield values that span tens of ‰ over our experimental temperature range. Even with strong constraints on the identity and proportions of secondary phases, with so much variation between $1/T–10^3\ln\alpha_{min\text{-}H2O}$ relationships, it is expected that ΔD between the bulk material and the vapor would evolve through time. Furthermore, isotope fractionation may not proceed at equilibrium during mineral growth. However, it is noteworthy that the magnitude of the $10^3\ln\alpha_{min\text{-}H2O}$ for hydrous phases correlates with the OH-stretching frequencies of a phase (Suzuoki and Epstein, 1976; Graham et al., 1980; Dobson et al., 1989). Zeolites, clays, and other hydrous silicate phases have OH-stretching frequencies that overlap with silicic glass, suggesting they are likely to have $10^3\ln\alpha_{min\text{-}H2O}$ values within ±10‰ of $10^3\ln\alpha_{gl\text{-}H2O}$ (Dobson et al., 1989).

4.3. Repartitioning of H_2O_m to OH

In experiments for which there are speciation data from FTIR measurements (Fig. 7), the proportion of OH^- in H_2O_t is ~1.0 wt % in LSR glass hydrated for 48 h at 375 °C, which is very close to the equilibrium speciation predicted by Ihinger et al. (1999), whose models extend down to 400 °C. This near match may suggest that the repartitioning of the diffusive species (H_2O_m) into OH^- is near equilibrium (Fig. 11). Other recent experimental data plotted in Fig. 11a show relationships between OH^- and H_2O_t that are more linear between 150 and 300 °C. The solid black symbols are FTIR data from wet fault gouge experiments run at 300 °C and regardless of the extent of hydration, the OH^-/H_2O_m ratios remain consistent (Table S4; Proctor et al., 2017). These data, along with those from hydration experiments by Cullen et al. (2019), have a positive linear correlation with temperature (Fig. 11b). The 200 °C data are consistent with expected OH^- and H_2O_t concentrations extrapolated from high temperature relationships (Ihinger et al., 1999). However, their 250 °C experiment yields higher OH^- concentrations than predicted, causing a temperature estimate ~70 °C in excess of the 250 °C curve. The linear relationship of temperature and OH^-/H_2O_m ratios in these two studies

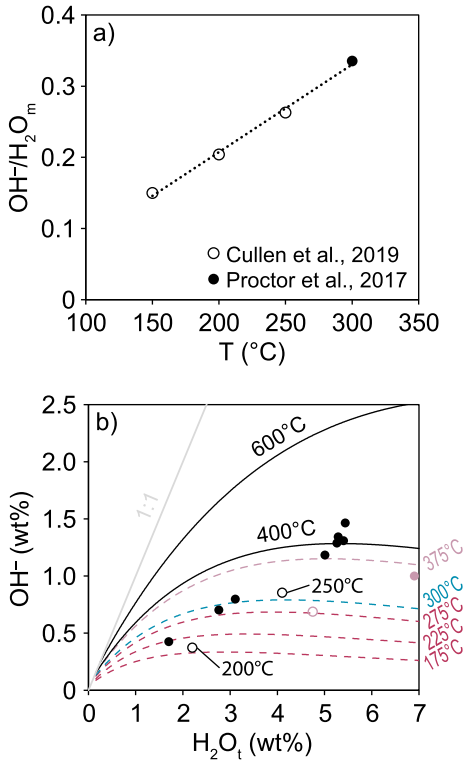

Fig. 11. H_2O speciation results from experimental rhyolitic glass. (a) OH^-/H_2O_m ratios appear to have a linear relationship with T at all concentrations (Cullen et al., 2019; Proctor et al., 2017). This ratio does not change with bulk H_2O contents between 1.5 and 5.0 wt% in the fault gouge experiments of Proctor et al. (2017) at 300 °C (b). Solid curves show equilibrium OH^- concentrations as a function of T and H_2O_t from Ihinger et al. (1999). Dashed curves are extrapolations of the Ihinger relationship to sub-magmatic T. Solid pink circle (a) is from the 48 h-long 375 °C experiment (Fig. 7). Open pink circle maintains OH^-/H_2O_m ratio from FTIR, but adjusts H_2O_t to the concentration measured by TC/EA.

suggests that the H_2O speciation below the glass transition, T_g, may be controlled by a fundamentally different mechanism than above T_g in a melt-like regime.

4.4. Model fits to data

We develop a finite difference reaction–diffusion model and apply it to our data (Figs. 12 and 13). Briefly, the numerical code models diffusion of H_2O_m and HDO_m into the glass, and at each timestep, these are allowed to repartition to OH^- and OD^- according to the reactions:

$$H_2O_m\ (glass) + O\ (glass) \underset{k_{-1}}{\overset{k_{+1}}{\rightleftharpoons}} 2OH^-\ (glass), \quad (4)$$

$$HDO_m\ (glass) + O\ (glass) \underset{a_{-1}}{\overset{0.5a_{+1}}{\rightleftharpoons}} OD^-\ (glass) + OH^-\ (glass), \quad (5)$$

$$HDO_m\ (glass) + O\ (glass) \underset{a_{-1}}{\overset{0.5a_{+1}}{\rightleftharpoons}} OH^-\ (glass) + OD^-\ (glass), \quad (6)$$

and

$$D_2O_m\ (glass) + O\ (glass) \underset{b_{-1}}{\overset{b_{+1}}{\rightleftharpoons}} 2OD^-\ (glass). \quad (7)$$

where the k's are reaction rate constants. A large k_{+1} implies fast exchange kinetics and equilibrium speciation, whereas a small k_{+1} implies that none of the H_2O_m diffusing in gets repartitioned to OH^-. Although the second and third reactions (Eqs. (5) and (6)) appear to be identical, the two H-bearing products of the reaction need to be treated as separate species for isotope mass balance purposes. The full derivation and validation of the isotope diffusion–reaction model are presented in the Supplementary Materials (Text S1) and model parameters are given in Table S5.

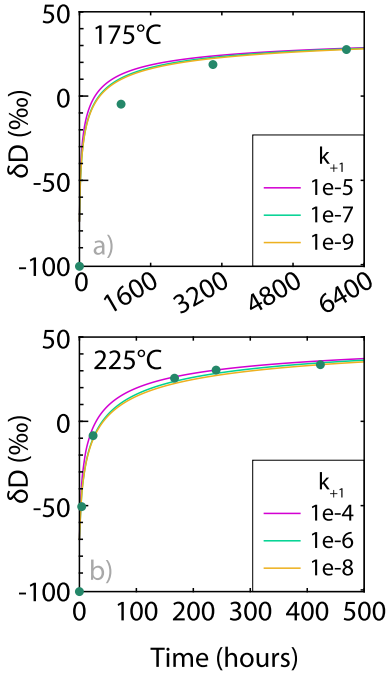

Fig. 12. Preferred model fits to the experimental δD_{gl} time series for (a) 175 °C and (b) 225 °C. Boundary conditions for the models are given in Table S6.

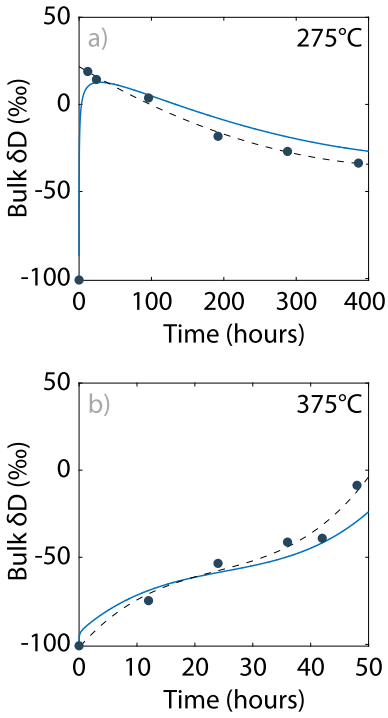

Fig. 13. Model fits (solid curves) to the experimental δD_{gl} time series for (a) 275 °C and (b) 375 °C require a δD boundary condition that changes through time. The δD boundary condition is set as the polynomial fit to the time-δD_{gl} results (dash lines).

4.4.1. Model results for a local equilibrium boundary condition

In the simplest version of the model, which is used as a reference scenario, we employ a local equilibrium boundary condition, meaning that we neglect changes occurring at the surface of the glass for simplicity and assume H_2O_m in the glass and vapor are in equilibrium: glass is 0.08 wt% H_2O_t and −100.8‰ δD_{gl}. At the boundary, OH^- and OD^- are not necessarily in equilibrium, but rather, increase at the boundary at a rate that depends on k_{+1}. The initial and boundary conditions are given in Table S6 and apply to the curves in Fig. 12 and Fig. S2.

The local equilibrium assumption yields acceptable fits to our data below 250 °C (Fig. 12). However, model fits to the bulk glass δD_{gl} data are unable to discriminate between near instantaneous, intermediate, and sluggish reaction rates between H_2O_m and OH^- as they all produce similar $\Delta D_{gl\text{-}H2O}$ results (Fig. 12a, b). This lends support to the interpretation that the experimental results <250 °C represent equilibrium isotope fractionation during glass hydration as kinetic effects are not able to induce changes in the δD_{gl} composition beyond analytical error. Modeled bulk H_2O_t concentrations through time are somewhat sensitive to the forward k_{+1} reaction rate (Fig. S3), but this can be compensated for by small increases in H_2O solubility or diffusivity and does not strongly affect bulk δD_{gl} evolution in the model. One possible reason the model is relatively insensitive to internal kinetic effects is that relatively low equilibrium OH^-/H_2O_m ratios may not leverage a large enough influence on the δD of H_2O_m at these temperatures (Fig. 11; Ihinger et al., 1999; Zhang, 2008).

The model curves in Fig. 12 use $10^3\alpha_{gl\text{-}H2O}$ values of approximately −33‰ and −25‰ at 175 °C and 225 °C, respectively, and represent equilibrium fractionation at these lower hydration temperatures. In both cases an $\alpha_{OH\text{-}H2Om}$ of 0.960 is assumed, and the main effect of changing this parameter is that $\alpha_{H2Om\text{-}vapor}$ adjusts accordingly at the boundary. The modeled $10^3\ln\alpha_{gl\text{-}H2O}$ for these two lower temperature experiments are more consistent with the hypothesis that D/H fractionations between glass and H_2O

vapor should increase towards 0‰ with increasing temperature, but to a lesser degree than previously estimated (Hudak and Bindeman, 2018). On the other hand, the model is unable to fit the data at temperatures above 250 °C by modulating reaction rate (k_{+1}) or mass-dependent kinetic fractionation (a_{+1}/k_{+1}) alone (Fig. S2). For example, the effect of reaction rates is greatest at the highest temperature (375 °C) where the glass has been fully hydrated. It results in a 9‰ spread in the bulk δD_{gl} over the modeled timescales at 375 °C, 4.5‰ at 275 °C, and <2‰ below 250 °C. Instead, these non-monotonic increases in bulk δD_{gl} data reveal that the bulk δD_{gl} mimics the δD at the glass-vapor boundary. This suggests that applying a local equilibrium boundary condition is not valid in the high temperature experiments, consistent with the observations of alteration and dissolution.

4.4.2. Relaxing the local equilibrium boundary condition

Our multiple numerical trials to fit the experimental data only fit the high temperature δD_{gl} evolution through time if there is a change in the δD boundary condition. The local equilibrium boundary condition requires that the glass-vapor boundary is not physically changing through time, an assumption that is contradicted by the SEM images showing partial dissolution of the glass and formation of secondary phases in the high temperature experiments. We use a polynomial fit to the bulk δD_{gl} data as a first approximation of the time evolution of the δD at the boundary. Fig. 13 shows polynomial fits (dashed lines) to the bulk δD_{gl} data that are then applied as time-dependent boundary condition. The resulting model outputs (solid curves) use the same $\alpha_{OH\text{-}H2Om}$ and a_{+1}/k_{+1} values as the models in Fig. 12 at intermediate values of k_{+1}. Once again, relatively slow or fast kinetics produce similar fits to the data. Overall, these results show how the bulk δD_{gl} closely mimics the time-evolving δD at the boundary. The fact that the high temperature experiments never reached a plateau in δD_{gs} can be attributed to ongoing reactions at the glass-vapor interface.

4.5. Summary of D/H fractionation in the glass-H_2O system

A primary goal of these experiments was to constrain equilibrium $10^3\ln\alpha_{gl\text{-}H2O}$ between silicic volcanic glass and H_2O vapor over the hydrothermal temperature range below the glass transition. The results of this study demonstrate that complex reactions on the glass surface (alteration and dissolution) and/or in the glass interior (water respeciation of H_2O_m to OH^-) make it difficult to obtain equilibrium fractionation factors, particularly at high temperatures over prolonged durations. Nevertheless, the experimental results and isotope diffusion modeling constrain equilibrium $10^3\alpha_{gl\text{-}H2O}$ values of −33 ± 5‰ at 175 °C and −25 ± 5‰ at 225 °C. Fig. 14 shows the existing hydrogen isotope literature $10^3\ln\alpha$ data for low temperature glass-H_2O and magmatic temperature OH-vapor and H_2O_m-vapor. These results are very close to fractionations observed in natural glasses, which find a $10^3\ln\alpha_{gl\text{-}H2O}$ of −33‰ for Earth surface temperatures (blue box; Friedman et al., 1993a; Seligman et al., 2016) and ~−30‰ around 100 °C (purple box; Hudak and Bindeman, 2018). At low temperatures, H_2O in glass is almost entirely H_2O_m, so Hudak and Bindeman (2018) uses the H_2O_m-vapor fractionations of Dobson et al. (1989; blue circles) to extrapolate $10^3\ln\alpha_{gl\text{-}H2O}$ across an intermediate temperature range, assuming no H_2O_m repartitioned below T_g. Here we interpret this to reflect a $10^3\ln\alpha$ relationship for H_2O_m-vapor rather than for bulk glass-H_2O (Fig. 14, blue curve). A linear extrapolation of $10^3\ln\alpha_{OH\text{-}vapor}$ from magmatic temperatures (green circles; Dobson et al., 1989) yields a range of ~−70‰ to −80‰ between 175 °C and 225 °C.

Evidence for repartitioning in our experiments and in other studies indicate that a $10^3\ln\alpha_{gl\text{-}H2O}$ should depend on the OH^-/H_2O_m ratio of the glass, determined by the kinetics of

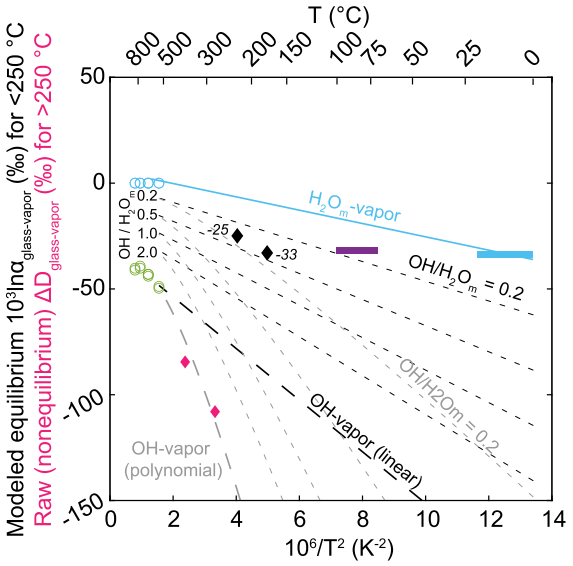

Fig. 14. $1/T^2 - 10^3\ln\alpha$ relationships in the glass/melt-H_2O system. Blue curve is a reinterpretation of the bulk glass-H_2O relationship of Hudak and Bindeman (2018) as a H_2O_m-vapor relationship extrapolated between low T (−33‰; Friedman et al., 1993b; Seligman et al., 2016) and high T (~0‰; Dobson et al., 1989). Purple box for glass-H_2O at 100 °C recorded in natural samples (Hudak and Bindeman, 2018). Dashed curves represent theoretical bulk glass-H_2O fractionations at various OH^-/H_2O_m ratios in glass or melt. Pink diamonds are raw data from experiments (see Fig. 5) and black diamonds are model results (Fig. 12). Results from below <250 °C are generally consistent with measured and expected OH^-/H_2O_m ratios while >250 °C results are consistent only with OH-dominated systems and an extreme extrapolation of Dobson et al. (1989) OH-vapor fractionations (green circles) to submagmatic T.

repartitioning. Grey and black dashed curves represent expected $1/T^2$—$10^3\ln\alpha_{gl\text{-}H2O}$ relationships at various OH^-/H_2O_m ratios. The 175 °C and 225 °C model results (black diamonds) mostly fall below OH^-/H_2O_m ratios of 0.5 or 0.2 depending on which OH-vapor extrapolation is used. This is broadly consistent with the expected OH^-/H_2O_m ratios from Cullen et al. (2019) and Proctor et al. (2017) shown in Fig. 11. By contrast, the $\Delta D_{gl\text{-}H2O}$ values from >250 °C are only consistent with the more extreme polynomial $10^3\ln\alpha_{OH\text{-}vapor}$ extrapolation of Dobson et al. (1989). This may indicate that the boundary layer on the glass regulating diffusion of H_2O into the glass and exchange between the glass and the H_2O vapor is dominated by very isotopically negative OH^- on the glass surface. We find this to be the most plausible explanation for our extreme $\Delta D_{gl\text{-}H2O}$ since alteration mineral assemblages should not have D/H fractionations that are too different from glass. This is because OH^- stretching frequencies largely control the magnitude of the D/H fractionation in minerals that have hydrogen bonds (e.g. Dobson et al., 1989; Graham et al., 1980; Méheut et al., 2010). Furthermore, this is consistent with a major conclusion of the modeling – that the δD of the glass boundary is the primary control on bulk δD_{gl}. The FTIR results for the fully hydrated glasses at 375 °C yield an OH^-/H_2O_m ratio of ~0.2, so an OH^- rich boundary could reconcile this relatively low measured OH^-/H_2O_m ratio with the extreme $\Delta D_{gl\text{-}H2O}$ values that are achieved above 250 °C.

4.6. Applications to natural systems

Untangling the proportion of secondary water added to ash or pumice after an eruption and its effect on the hydrogen isotope composition of the glass is the primary motivation for this work. Hydrogen isotopes and H_2O speciation are the two primary ways to differentiate between magmatic and secondary water. This work evaluates the possible implications of various glass cooling rates in water-rich environments during and following eruptions (Fig. 1).

At high temperatures, the timescales of hydration are short (Fig. 1). For instance, pumice clasts from the 2012 submarine eruption of Havre Volcano in the Kermadec Arc have high H_2O concentrations at the rims of vesicle bubble walls and low H_2O in the interior. Diffusion profiles are of sufficient length that high temperatures are required, so Mitchell et al. (2018) argue for ~400 °C hydration temperatures on the scale of a few minutes, which is corroborated by H isotope systematics in these and other, older submarine rhyolites (Mitchell et al., 2022). Similarly, Hudak et al. (2021) identify a rehydration trend by glacial meltwater during the 2009 eruption of Redoubt Volcano in Alaska, which they model to occur on timescales of tens of seconds. Hydrogen isotopes can therefore record magma-water in submarine or magma-ice interactions in subglacial settings, but only in highly fragmented or porous materials given the short timescales. Long timescale, high temperature glass-water interactions will result in glass alteration. In natural settings where this occurs, such as in the fumarolic cracks that gave the Valley of Ten Thousand Smokes (VTTS) in Alaska its name, temperatures over 250 °C sustained for at least a decade (Griggs, 1922) led to pervasive alteration (Papike, 1992; Kodosky and Keith, 1993, 1995).

Lower temperatures may be sustained much longer in some settings. However, the finite element modeling of cooling ignimbrites shows that the latent heat from the phase transition between vapor and liquid water fixes the temperature at the boiling point within ignimbrites for prolonged periods of time (Keating, 2005). Modeling of closure temperatures for H_2O diffusion in thin bubble walls further suggest that ~100 °C is a more likely hydration temperature (Hudak and Bindeman, 2020). Indeed, hydration temperatures near the boiling point of water for a given pressure have been recorded in pyroclastic density current deposits from eruptions of ~1 km^3 at Mount St. Helens (Seligman et al., 2018) to tens of km^3 at the VTTS and Crater Lake (Hudak and Bindeman, 2018) to super-eruptions like the Bishop Tuff (Randolph-Flagg et al., 2017).

Finally, the isotope reaction–diffusion model of water and glass could be further constrained by, and applied to, higher temperature glasses and melts. Discrete domains of textures and H_2O and CO_2 concentrations within obsidian pyroclasts indicate they are incrementally assembled by sintering of ash on the walls of volcanic conduits *syn*-eruptively (Castro et al., 2014; Watkins et al., 2016; Gardner et al., 2017). Volatile diffusion studies give timescales of pyroclast assembly (Watkins et al., 2016, 2017) and decompression histories (Watkins et al., 2012). These types of samples and processes could be good targets for constraining hydrogen isotope fractionation between OH-H_2O_m using our model because the model domain within a pyroclast could be chosen far from any changing melt-vapor interface. Giachetti et al. (2020) made a step in this direction. Melt embayments are increasingly used to constrain magma decompression and ascent rates (Humphreys et al., 2008; Lloyd et al., 2014; Ferguson et al., 2016; Myers et al., 2016, 2018; Moussallam et al., 2019). These could be a good complement for constraining this fractionation as well as the H_2O_m-vapor fractionation since one boundary in that system is open to devolatilization and the change in H_2O_t and OH/H_2O_m equilibrium are well understood at those conditions. Isotope diffusion in embayments may additionally help discriminate among different decompression histories that produce similar H_2O_t profiles from the vapor bubble inward.

5. Conclusions

(1) Below 250 °C, the time evolution of bulk glass δD_{gl} is asymptotic, approaching the equilibrium δD_{gl} composition with the H_2O vapor. This contrasts with the time series of δD_{gl} in experiments conducted above 250 °C that record strong δD_{gl} depletions that do not evolve asymptotically towards a single value and represent disequilibrium between glass and vapor.

(2) At 375 °C, the glasses have up to 1.0 wt% of OH^- distributed homogenously throughout the fully hydrated glass. This reaffirms observations in both experimental studies (Proctor et al., 2017; Cullen et al., 2019) and in natural samples (Bindeman and Lowenstern, 2016) that document water repartitioning and OH^- formation below the glass transition temperature.

(3) We develop an isotope-reaction model for hydrogen during volcanic glass hydration that incorporates the internal reaction $H_2O_m + O \rightleftharpoons 2OH^-$ during glass hydration. Modeled $10^3 ln\alpha_{gl\text{-}H2O}$ for D/H are approximately −33‰ and −25‰ at 175 °C and 225 °C, respectively. These results suggest that equilibrium H isotope fractionation changes more modestly, if at all, with increasing temperature than previously estimated (Hudak and Bindeman, 2018). At these conditions, the model cannot distinguish between fast or slow reaction kinetics for $H_2O_m + O \rightleftharpoons 2OH^-$.

(4) The time evolution of bulk δD_{gl} in experiments above 250 °C record strong depletions that cannot be explained by reasonable parameters in our isotope reaction–diffusion model. However, we are able to exclude multiple hypotheses in isolation for the observed δD_{gl} depletions including: (i) simple equilibrium $10^3 ln\alpha_{gl\text{-}H2O}$ fractionations between glass and vapor, (ii) kinetic isotope effects associated with diffusion of isotopologues of H_2O (or H_2 or H^+) of different masses, and (iii) a diffusion–reaction model that assumes local equilibrium to govern incomplete chemical reactions between H_2O_m and OH^- within glass.

(5) Model behavior is most sensitive to changes in the boundary condition and suggests that formation of the required thin layer of isotopically negative OH^- groups on the surface may be a result of some combination glass dissolution and secondary mineral formation on the glass surface, regulate the bulk δD_{gl} of the glasses at 275 °C and 375 °C. While intermediate values for the forward reaction rate, k_{+1}, do produce the apparent overshoot of the equilibrium δD_{gl} observed at 275 °C (Fig. S2), this is likely of secondary importance relative to changes in the glass boundary condition.

(6) We suggest that this H isotope reaction–diffusion model has broad application to volatile diffusion at higher temperatures which may shed light on conduit processes. In both cases, boundary conditions can be ignored (e.g., obsidian pyroclasts) or the boundary can be designed to evolve according to well constrained OH^-/H_2O_m and H_2O_t as a function of P-T-X_{H2O} (e.g. melt embayments).

Data availability

Data is provided at: https://doi.org/10.7910/DVN/XW8NPB

Declaration of Competing Interest

The authors declare that they have no known competing financial interests or personal relationships that could have appeared to influence the work reported in this paper.

Acknowledgements

We thank J. Palandri for assistance in the stable isotope lab and J. Chouinard for help on the EPMA. We extend a special thanks to B. Proctor for allowing us to publish FTIR data from his experimental work. We appreciate the thoughtful and constructive comments from Associate Editor L. Anovitz, C. Aubaud, P. Shanks, and four

other anonymous reviewers, which greatly improved this manuscript. This work was supported by an NSF grant, EAR 1822977, to I. Bindeman. Any use of trade, firm, or product names is for descriptive purposes only and does not imply endorsement by the U.S. Government.

Data availability

Supplementary Data Tables and the MATLAB model are provided in the Supplemental Material and in a Data Repository at https://doi.org/10.7910/DVN/XW8NPB.

Appendix A. Supplementary material

Supplementary material to this article can be found online at https://doi.org/10.1016/j.gca.2022.09.032.

References

Anovitz, L.M., Elam, J.M., Riciputi, L.R., Cole, D.R., 2004. Isothermal time-series determination of the rate of diffusion of water in Pachuca obsidian. Archaeometry 2, 301–326.
Anovitz, L.M., Cole, D.R., Fayek, M., 2008. Mechanisms of rhyolitic glass hydration below the glass transition. Am. Mineral. 93, 1166–1178.
Bakel, A., Ebert, W., Luo, J., 1995. Long-term performace of glasses for Hanford low-level waste. Ceram. Trans. 61, 515–522.
Bates, J.K., Jardine, L.J., Steindler, M.J., 1982. Hydration Aging of Nuclear Waste Glass. Science 218 (80), 51–54.
Bates, J.K., Steindler, M.J., 1982. Alteration of Nuclear Waste by Hydration. MRS Online Proc. Libary 15, 83–90.
Behrens, H., Zhang, Y., Leschik, M., Wiedenbeck, M., Heide, G., Frischat, G.H., 2007. Molecular H_2O as carrier for oxygen diffusion in hydrous silicate melts. Earth Planet. Sci. Lett. 254, 69–76.
Bindeman, I.N., Hudak, M.R., Palandri, J.P., Qi, H., Milovsky, R., Hervig, R.L., Perfit, M. R., 2021. Rhyolitic and basaltic reference materials for TC/EA analysis: Investigation of water extraction and D/H ratios. Chem. Geol. 583, 120486.
Bindeman, I.N., Lowenstern, J.B., 2016. Low-δD hydration rinds in Yellowstone perlites record rapid syneruptive hydration during glaical and interglacial conditions. Contrib. Mineral. Petrol. 171, 1–24.
Cassel, E.J., Breecker, D.O., 2017. Long-term stability of hydrogen isotope ratios in hydrated volcanic glass. Geochim. Cosmochim. Acta 200, 67–86.
Cassel, E.J., Graham, S.A., Chamberlain, C.P., 2009. Cenozoic tectonic and topographic evolution of the northern Sierra Nevada, California, through stable isotope paleoaltimetry in volcanic glass. Geology 37, 547–550.
Cassel, E.J., Graham, S.A., Chamberlain, C.P., Henry, C.D., 2012. Early Cenozoic topography, morphology, and tectonics of the northern Sierra Nevada and western Basin and Range. Geosphere 8, 229–249.
Cassel, E.J., Breecker, D.O., Henry, C.D., Larson, T.E., Stockli, D.F., 2014. Profile of a paleo-orogen: High topography across the present-day Basin and Range from 40 to 23 Ma. Geology 42, 1007–1010.
Castro, J.M., Bindeman, I.N., Tuffen, H., Ian, S.C., 2014. Explosive origin of silicic lava: Textural and δD-H_2O evidence for pyroclastic degassing during rhyolite effusion. Earth Planet. Sci. Lett. 405, 52–61.
Cerling, T.E., Brown, F.H., Bowman, J.R., 1985. Low-temperature alteration of volcanic glass: hydration, Na, K, ^{18}O and Ar mobility. Chem. Geol. 52, 281–293.
Colwyn, D.A., Hren, M.T., 2019. An abrupt decrease in Southern Hemisphere terrestrial temperature during the Eocene-Oligocene transition. Earth Planet. Sci. Lett. 512, 227–235.
Coumans, J.P., Llewellin, E.W., Humphreys, M.C.S., Nowak, M., Brooker, R.A., Mathias, S.A., McIntosh, I.M., 2020. An experimentally-validated numerical model of diffusion and speciation of water in rhyolitic silicate melt. Geochim. Cosmochim. Acta 276, 219–238.
Cullen, J.T., Hurwitz, S., Barnes, J.D., Lassiter, J.C., Penniston-Dorland, S., Kasemann, S.A., Thordsen, J.J., 2019. Temperature-dependent variations in mineralogy, major element chemistry and the stable isotopes of boron, lithium and chlorine resulting from hydration of rhyolite: Constraints from hydrothermal experiments at 150 to 350 °C and 25 MPa. Geochim. Cosmochim. Acta 261, 269–287.
Declercq, J., Diedrich, T., Perrot, M., Gislason, S.R., Oelkers, E.H., 2013. Experimental determination of rhyolitic glass dissolution rates at 40–200°C and 2<pH<10.1. Geochim. Cosmochim. Acta 100, 251–263.
Del Gaudio, P., Behrens, H., Deubener, J., 2007. Viscosity and glass transition temperature of hydrous float glass. J. Non. Cryst. Solids 353, 223–236.
Dettinger, M.P., Quade, J., 2015. Testing the analytical protocols and calibration of volcanic glass for the reconstruction of hydrogen isotopes in paleoprecipitation. Mem. Geol. Soc. Am. 212, 261–276.
Dingwell, D.B., 1998. The glass transition in hydrous granitic melts. Phys. Earth Planet. Inter. 107, 1–8.
Dingwell, D.B., Romano, C., Hess, K.U., 1996. The effect of water on the viscosity of a haplogranitic melt under P-T-X conditions relevant to silicic volcanism. Contrib. Mineral. Petrol. 124, 19–28.
Dingwell, D.B., 1995. Relaxation in silicate melts: some applications. In: Reviews in Mineralogy and Geochemistry: Structure, Dynamics and Properties of Silicate Melts, pp. 21–66.
Dobson, P.F., Epstein, S., Stolper, E.M., 1989. Hydrogen isotope fractionation between coexisting vapor and silicate glasses and melts at low pressure. Geochim. Cosmochim. Acta 53, 2723–2730.
Ferguson, D.J., Gonnermann, H.M., Ruprecht, P., Plank, T., Hauri, E.H., Houghton, B.F., Swanson, D.A., 2016. Magma decompression rates during explosive eruptions of Kīlauea volcano, Hawaii, recorded by melt embayments. Bull. Volcanol. 78, 1–12.
Fournier, M., Gin, S., Frugier, P., 2014. Resumption of nuclear glass alteration: State of the art. J. Nucl. Mater. 448, 348–363.
Fournier, M., Gin, S., Frugier, P., Mercado-Depierre, S., 2017. Contribution of zeolite-seeded experiments to the understanding of resumption of glass alteration. npj Mater. Degrad. 1, 1–12.
Friedman, I., Gleason, J., Sheppard, R.A., Gude, A.J., 1993a. Deuterium Fractionation as Water Diffuses into Silicic Volcanic Ash. In: Swart, P.K., Lohmann, K.C., Mckenzie, J., Savin, S. (Eds.), Climate Change in Continental Isotopic Records, pp. 321–323.
Friedman, I., Gleason, J., Warden, A., 1993b. Ancient climate from deuterium content of water in volcanic glass. In: Swart, P.K., Lohmann, K.C., Mckenzie, J., Savin, S. (Eds.), Climate Change in Continental Isotopic Records, pp. 309–319.
Friedman, I., Long, W., 1976. Hydration Rate of Obsidian. Science 191, 347–352.
Gardner, J.E., Llewellin, E.W., Watkins, J.M., Befus, K.S., 2017. Formation of obsidian pyroclasts by sintering of ash particles in the volcanic conduit. Earth Planet. Sci. Lett. 459, 252–263.
Gazis, C., Taylor, H.P., Hon, K., Tsvetkov, A., 1996. Oxygen isotopic and geochemical evidence for a short-lived, high-temperature hydrothermal event in the Chegem caldera, Caucasus Mountains, Russia. *J. Volcanol. Geotherm. Res.* 73, 213–244.
Giachetti, T., Gonnermann, H.M., Gardner, J.E., Shea, T., Gouldstone, A., 2015. Discriminating secondary from magmatic water in rhyolitic matrix-glass of volcanic pyroclasts using thermogravimetric analysis. Geochim. Cosmochim. Acta 148, 457–476.
Giachetti, T., Hudak, M.R., Shea, T., Bindeman, I.N., Hoxsie, E.C., 2020. D/H ratios and H2O contents record degassing and rehydration history of rhyolitic magma and pyroclasts. Earth Planet. Sci. Lett. 530, 115909.
Gin, S., Jollivet, P., Fournier, M., Angeli, F., Frugier, P., Charpentier, T., 2015. Origin and consequences of silicate glass passivation by surface layers. Nat. Commun. 6, 1–8.
Gin, S., Collin, M., Jollivet, P., Fournier, M., Minet, Y., Dupuy, L., Mahadevan, T., Kerisit, S., Du, J., 2018. Dynamics of self-reorganization explains passivation of silicate glasses. Nat. Commun. 9, 1–9.
Gin, S., Delaye, J.M., Angeli, F., Schuller, S., 2021. Aqueous alteration of silicate glass: state of knowledge and perspectives. npj Mater. Degrad. 5, 1–20.
Giordano, D., Nichols, A.R.L., Dingwell, D.B., 2005. Glass transition temperatures of natural hydrous melts: A relationship with shear viscosity and implications for the welding process. J. Volcanol. Geotherm. Res. 142, 105–118.
Graham, C.M., Sheppard, S.M.F., Heaton, T.H.E., 1980. Experimental hydrogen isotope studies-I. Systematic of hydrogen isotope fractionation in the systems epidote-H_2O, and AlO(OH)-H_2O. Geochim. Cosmochim. Acta 44, 353–364.
Griggs, R.K., 1922. The Valley of Ten Thousand Smokes. The National Geographic Society, Washington.
Hellmann, R., Cotte, S., Cadel, E., Malladi, S., Karlsson, L.S., Lozano-Perez, S., Cabié, M., Seyeux, A., 2015. Nanometre-scale evidence for interfacial dissolution-reprecipitation control of silicate glass corrosion. Nat. Mater. 14, 307–311.
Holt, E.W., Taylor, H.P., 2001. $^{18}O/^{16}O$ studies of fossil fissure fumaroles from the Valley of Ten Thousand Smokes, Alaska. *Bull. Volcanol.* 63, 151–163.
Horita, J., Wesolowski, D.J., 1994. Liquid-vapor fractionation of oxygen and hydrogen isotopes of water from the freezing to the critical temperature. Geochim. Cosmochim. Acta 58, 3425–3437.
Hudak, M.R., Bindeman, I.N., 2018. Conditions of pinnacle formation and glass hydration in cooling ignimbrite sheets from H and O isotope systematics at Crater Lake and the Valley of Ten Thousand Smokes. Earth Planet. Sci. Lett. 500, 56–66.
Hudak, M.R., Bindeman, I.N., 2020. Solubility, diffusivity, and O isotope systematics of H_2O in rhyolitic glass in hydrothermal temperature experiments. Geochim. Cosmochim. Acta 283, 222–242.
Hudak, M.R., Bindeman, I.N., Loewen, M.W., Giachetti, T., 2021. Syn-Eruptive Hydration of Volcanic Ash Records Pyroclast-Water Interaction in Explosive Eruptions. Geophys. Res. Lett. 48, 1–8.
Humphreys, M.C.S., Menand, T., Blundy, J.D., Klimm, K., 2008. Magma ascent rates in explosive eruptions: Constraints from H_2O diffusion in melt inclusions. Earth Planet. Sci. Lett. 270, 25–40.
Ihinger, P.D., Zhang, Y., Stolper, E.M., 1999. The speciation of dissolved water in rhyolitic melt. Geochim. Cosmochim. Acta 63, 3567–3578.
Jackson, L.J., Horton, B.K., Beate, B.O., Bright, J., Breecker, D.O., 2019. Testing stable isotope paleoaltimetry with Quaternary volcanic glasses from the Ecuadorian Andes. Geology 47, 411–414.
Jollivet, P., Angeli, F., Cailleteau, C., Devreux, F., Frugier, P., Gin, S., 2008. Investigation of gel porosity clogging during glass leaching. J. Non. Cryst. Solids 354, 4952–4958.
Karlsson, H.R., Clayton, R.N., 1990. Oxygen and hydrogen isotope geochemistry of zeolites. Geochim. Cosmochim. Acta 54, 1369–1386.

Keating, G.N., 2005. The role of water in cooling ignimbrites. J. Volcanol. Geotherm. Res. 142, 145–171.
Kodosky, L.G., Keith, T.E.C., 1993. Factors controlling the geochemical evolution of fumarolic encrustations, Valley of Ten Thousand Smokes, Alaska. *J. Volcanol. Geotherm. Res.* 55, 185–200.
Kodosky, L.G., Keith, T.E.C., 1995. Further insights into the geochemical evolution of fumarolic alteration, Valley of Ten Thousand Smokes, Alaska. *J. Volcanol. Geotherm. Res.* 65, 181–190.
Lambert, S.J., Epstein, S., 1980. Stable isotope investigations of an active geothermal system in Valles Caldera, Jemez Mountains, New Mexico. J. Volcanol. Geotherm. Res. 8, 111–129.
Liu, Y., Zhang, Y., Behrens, H., 2005. Solubility of H_2O in rhyolitic melts at low pressures and a new empirical model for mixed H_2O-CO_2 solubility in rhyolitic melts. J. Volcanol. Geotherm. Res. 143, 219–235.
Lloyd, A.S., Ruprecht, P., Hauri, E.H., Rose, W., Gonnermann, H.M., Plank, T., 2014. NanoSIMS results from olivine-hosted melt embayments: Magma ascent rate during explosive basaltic eruptions. J. Volcanol. Geotherm. Res. 283, 1–18.
Loewen, M.W., Bindeman, I.N., Melnik, O.E., 2017. Eruption mechanisms and short duration of large rhyolitic lava flows of Yellowstone. Earth Planet. Sci. Lett. 458, 80–91.
Lowenstern, J.B., Pitcher, B.W., 2013. Analysis of H_2O in silicate glass using attenuated total refectance (ATR) micro-FTIR spectroscopy. Am. Mineral. 98, 1660–1668.
Majérus, O., Lehuédé, P., Biron, I., Alloteau, F., Narayanasamy, S., Caurant, D., 2020. Glass alteration in atmospheric conditions: crossing perspectives from cultural heritage, glass industry, and nuclear waste management. npj Mater. Degrad. 4, 1–24.
Martin, E., Bindeman, I., Balan, E., Palandri, J., Seligman, A., Villemant, B., 2017. Hydrogen isotope determination by TC/EA technique in application to volcanic glass as a window into secondary hydration. J. Volcanol. Geotherm. Res. 348, 49–61.
Mazer, J.J., Stevenson, C.M., Ebert, W.L., Bates, J.K., 1991. The experimental hydration of obsidian as a function of relative humidty and temperature. Am. Antiq. 56, 504–513.
Méheut, M., Lazzeri, M., Balan, E., Mauri, F., 2010. First-principles calculation of H/D isotopic fractionation between hydrous minerals and water. Geochim. Cosmochim. Acta 74, 3874–3882.
Mitchell, S.J., McIntosh, I.M., Houghton, B.F., Carey, R.J., Shea, T., 2018. Dynamics of a powerful deep submarine eruption recorded in H_2O contents and speciation in rhyolitic glass: The 2012 Havre eruption. Earth Planet. Sci. Lett. 494, 135–147.
Mitchell, S.J., Hudak, M.R., Bindeman, I.N., Carey, R.J., McIntosh, I.M., Houghton, B.F., Rubin, K.H., 2022. Isotopic signatures of magmatic fluids and seawater within silicic submarine volcanic deposits. Geochim. Cosmochim. Acta 326, 214–233.
Moussallam, Y., Rose-Koga, E.F., Koga, K.T., Médard, E., Bani, P., Devidal, J.L., Tari, D., 2019. Fast ascent rate during the 2017–2018 Plinian eruption of Ambae (Aoba) volcano: a petrological investigation. Contrib. Mineral. Petrol. 174, 1–24.
Myers, M.L., Wallace, P.J., Wilson, C.J.N., Morter, B.K., Swallow, E.J., 2016. Prolonged ascent and episodic venting of discrete magma batches at the onset of the Huckleberry Ridge supereruption, Yellowstone. *Earth Planet. Sci. Lett.* 451, 285–297.
Myers, M.L., Wallace, P.J., Wilson, C.J.N., Watkins, J.M., Liu, Y., 2018. Ascent rates of rhyolitic magma at the onset of three caldera-forming eruptions. Am. Mineral. 103, 952–965.
Neeway, J., Abdelouas, A., Grambow, B., Schumacher, S., Martin, C., Kogawa, M., Utsunomiya, S., Gin, S., Frugier, P., 2012. Vapor hydration of SON68 glass from 90 °C to 200 °C: A kinetic study and corrosion products investigation. J. Non. Cryst. Solids 358, 2894–2905.
Newman, S., Epstein, S., Stolper, E., 1988. Water, carbon dioxide, and hydrogen isotopes in glasses from the ca. 1340 A.D. eruption of the Mono Craters, California: Constraints on degassing phenomena and initial volatile content. J. Volcanol. Geotherm. Res. 35, 75–96.
Newman, S., Lowenstern, J.B., 2002. Volatile Calc: a silicate melt – H_2O – CO_2 solution model written in Visual Basic for excel. Comput. Geosci. 28, 597–604.
Ni, H., Zhang, Y., 2008. H_2O diffusion models in rhyolitic melt with new high pressure data. Chem. Geol. 250, 68–78.
Oelkers, E.H., 2001. General kinetic description of multioxide silicate mineral and glass dissolution. Geochim. Cosmochim. Acta 65, 3703–3719.
Papike, J.J., 1992. The valley of ten thousand Smokes, Katmai, Klaska: A unique geochemistry laboratory. Geochim. Cosmochim. Acta 56, 1429–1449.
Proctor, B.P., Lockner, D.A., Lowenstern, J.B., Beeler, N.M., 2017. Conversion of wet glass to melt at lower seismogenic zone conditions: implications for pseudotachylyte creep. Geophys. Res. Lett. 44, 1–8.
Randolph-Flagg, N., Breen, S., Hernandez, A., Manga, M., Self, S., 2017. Evenly spaced columns in the Bishop Tuff (California, USA) as relicts of hydrothermal cooling. Geology 45, 1015–1018.
Rempel, A.W., Bindeman, I.N., 2019. A model for the development of stable isotopic water signatures of tephra deposited on ice following subglacial caldera collapse. J. Volcanol. Geotherm. Res. 377, 131–145.
Seligman, A.N., Bindeman, I.N., Watkins, J.M., Ross, A.M., 2016. Water in volcanic glass: From volcanic degassing to secondary hydration. Geochim. Cosmochim. Acta 191, 216–238.
Seligman, A.N., Bindeman, I., Van Eaton, A., Hoblitt, R., 2018. Isotopic insights into the degassing and secondary hydration of volcanic glass from the 1980 eruptions of Mount St. Helens. *Bull. Volcanol.* 80, 1–18.
Sheppard, S.M.F., Gilg, H.A., 1996. Stable isotope geochemistry of clay minerals. Clay Miner. 31, 1–24.
Silver, L.A., Ihinger, P.D., Stolper, E., 1990. The influence of bulk composition on the speciation of water in silicate glasses. Contrib. Mineral. Petrol. 104, 142–162.
Stolper, E., 1982. Water in silicate glasses: An infrared spectroscopic study. Contrib. Mineral. Petrol. 81, 1–17.
Suzuoki, T., Epstein, S., 1976. Hydrogen isotope fractionation between OH-bearing minerals and water. Geochim. Cosmochim. Acta 40, 1229–1240.
Taylor, B.E., Eichelberger, J.C., Westrich, H.R., 1983. Hydrogen isotopic evidence of rhyolitic magma degassing during shallow intrusion and eruption. Nature 306, 541–545.
Vennemann, T.W., O'Neil, J.R., 1996. Hydrogen isotope exchange reactions between hydrous minerals and molecular hydrogen: I. A new approach for the determination of hydrogen isotope fractionation at moderate temperatures. Geochim. Cosmochim. Acta 60, 2437–2451.
Walter, S., Castro, J., 2020. VolcDeGas: A program for modelling hydrogen isotope fractionation during degassing of rhyolitic melts. Volcanica 3, 155–168.
Watkins, J.M., Manga, M., Depaolo, D.J., 2012. Bubble geobarometry: A record of pressure changes, degassing, and regassing at Mono Craters, California. Geology 40, 699–702.
Watkins, J.M., Gardner, J.E., Befus, K.S., 2016. Nonequilibrium degassing, regassing, and vapor fluxing in magmatic feeder systems. Geology 45, 183–186.
Watkins, J.M., DePaolo, D.J., Watson, E.B., 2017. Kinetic Fractionation of Non-Traditional Stable Isotopes by Diffusion and Crystal Growth Reactions. In: Reviews on Mineralogy & Geochemistry, pp. 85–125.
Withers, A.C., Zhang, Y., Behrens, H., 1999. Reconciliation of experimental results on H_2O speciation in rhyolitic glass using in-situ and quenching techniques. Earth Planet. Sci. Lett. 173, 343–349.
Zhang, Y., 1999. H_2O in rhyolitic glasses and melts: Measurement, speciation, solubility, and diffusion. Rev. G 37, 493–516.
Zhang, Y., 2008. Geochemical Kinetics. Princeton University Press.
Zhang, Y., Behrens, H., 2000. H_2O diffusion in rhyolitic melts and glasses. Chem. Geol. 169, 243–262.
Zhang, Y., Stolper, E.M., Wasserburg, G.J., 1991. Diffusion of water in rhyolitic glasses. Geochim. Cosmochim. Acta 55, 441–456.
Zhang, Y., Jenkins, J., Xu, Z., 1997. Kinetics of the reaction $H_2O + O \rightarrow 2OH$ in rhyolitic glasses upon cooling: Geospeedometry and comparison with glass transition. Geochim. Cosmochim. Acta 61, 2167–2173.